Petroleum Science 23 (2026) 4113–4131

Contents lists available at ScienceDirect

Petroleum Science

journal homepage: www.keaipublishing.com/en/journals/petroleum-science

Original Paper

Optimization of injection parameters in offshore low permeability reservoir based on a compositional embedded discrete fracture model

Shi-Qian Xu [a,b,*], Qi-Jun Zeng [a,b], Jian-Chun Guo [a,b,**], Rong-Hao Cui [c], Cong Lu [a,b], Wen-Jian Zhou [a,b], Qin-Ru Xue [a,b]

[a] *Petroleum Engineering School, Southwest Petroleum University, Chengdu, 610500, Sichuan, China*
[b] *State Key Laboratory of Oil and Gas Reservoir Geology and Exploitation, Southwest Petroleum University, Chengdu, 610500, Sichuan, China*
[c] *Earth Science and Engineering, Physical Science and Engineering (PSE) Division, King Abdullah University of Science and Technology (KAUST), Thuwal, 23955-6900, Saudi Arabia*

A R T I C L E I N F O

Article history:
Received 17 September 2025
Received in revised form
2 December 2025
Accepted 26 February 2026
Available online 5 March 2026

Edited by Meng-Jiao Zhou

Keywords:
Offshore low permeability
Embedded discrete fracture model
Injection parameter
Optimization
Low-velocity nonlinear flow

A B S T R A C T

Offshore development tends to aim for high production with fewer wells, which leads to large well spacing and wide range of low-pressure gradient. Compared with onshore, the low-velocity nonlinear flow, matrix stress sensitivity, and CO_2 miscibility have significant impacts on the injection optimization design. However, existing studies rarely examine the impact of these characteristics on injection parameters, including injection fluid selection, injection rate and timing. Therefore, we first establish a 3D embedded discrete fracture model for compositional simulation. Multiple mechanisms, including low-velocity nonlinear flow, matrix and fracture stress sensitivity are considered comprehensively. After evaluating the sweep area, injection capacity, and production performance of different injection fluid (H_2O, CO_2, N_2), a fluid selection strategy was proposed. The cumulative oil production under a certain water cut/gas-oil ratio is taken as the objective function. Then the injection rate and timing are studied. Results show that, when the injection rate of CO_2 and H_2O is high, the fluid breakthrough comes early. When the injection rate is low, the reservoir pressure is poorly maintained, resulting strong matrix stress sensitivity, and low CO_2 miscibility efficiency. Therefore, there is an optimal CO_2 and H_2O injection rate. In comparison with the traditional Darcy flow, the optimal H_2O injection rate is higher. The maximum difference reaches 11.1% with matrix permeability of 5×10^{-3} μm^2. As the matrix permeability increases, optimal CO_2 injection timing is gradually advanced. While the optimal H_2O injection timing is gradually delayed. The proposed 3D-EDFM compositional simulator can serve as an effective and reliable method for injection-production optimization.

1. Introduction

Offshore low-permeability oil and gas resources are abundant (Sun et al., 2024). The oil and gas-bearing strata are concentrated in the Paleogene and Archean strata of the Cenozoic Era in China. They are widely distributed in the Bohai Sea, the East China Sea and the South China Sea (mpared with onshore, offshore low-permeability development started late. With the rise in oil prices and new discoveries in exploration, development began in 2004. In recent years, the strategy of ensuring national energy security places high demands on the exploration and development of offshore oil and gas resources. As the main force for increasing reserves and production, it is imperative to promote the effective development of offshore low-permeability oil and gas fields (Xu et al., 2025a). However, unlike onshore oil fields, offshore oil and gas development requires large investment, high risk, and high single-well production requirements due to the marine operating environment. Offshore economic development requires high production with fewer wells (Zhao et al., 2025). This is in

* Corresponding author.
** Corresponding author.
E-mail addresses: xsq.s.upc@gmail.com (S.-Q. Xu), jianchunguo@yeah.net (J.-C. Guo).
Peer review under the responsibility of China University of Petroleum (Beijing).

https://doi.org/10.1016/j.petsci.2026.02.023
1995-8226/

contradiction with the low production of many wells on land. Therefore, it is difficult to directly learn from onshore experience (Hu et al., 2018).

The proven geological reserves of crude oil in offshore low-permeability sandstone reservoirs are nearly 600 million tons (Fig. 1(a)). Since the natural energy of block reservoirs is limited, water/gas injection development is needed to supplement energy (Zhang et al., 2021). At present, the permeability of the reservoirs that have been developed is mainly distributed in the range of 20–50 mD, accounting for more than 60%. The development method is mainly water drive. With the upgrading of offshore fracturing equipment, the development limit of offshore low-permeability oil reservoirs will be expanded. The crude oil production of new blocks is expected to increase significantly in the future (Fig. 1(b)) preparations for gas injection development should be made in advance (Yang et al., 2024). Therefore, it is urgent to study injection fluid selection and injection rate/time optimization for fractured vertical well flooding in offshore low permeability reservoir.

With the help of intelligent algorithms, there are many optimization technology studies on injection-production design in low permeability oil reservoirs. On the one hand, optimization algorithms are reliable tools for efficiently and automatically finding the optimal solution (Yang et al., 2025). Azamipour et al. (2018) improved genetic algorithm coupling with polytope search. Then it is used in injection and production schedule. The cyclic water injection (CWI) technique requires adjustment of injection volume, injection frequency, well shut-in time, production pressure at different stages for multiple wells. To efficiently optimize these operational parameters simultaneously. Sun et al. (2019) coupled a new hybrid optimization algorithm with a reservoir simulator to optimize CWI strategies for field applications. Utilizing PSO intelligent optimization algorithm, Ding et al. (2022) comprehensively studied CO_2 enhanced oil recovery and storage in low permeability oil reservoir. Including comparison between continuous gas injection, cyclic gas injection (CGI), and water alternating gas (WAG). Multi-objective optimization, tax credit of CO_2 stored on optimization results.

On the other hand, to improve the production prediction efficiency, some alternative reservoir simulation models have been proposed and further improved (Wang et al., 2021). Such as inter-well connectivity model (Zhou et al., 2021), machine learning-based surrogate model (Almasov and Onur, 2023) and so on. Lerlertpakdee et al. (2014) proposed a flow-network model to speed up reservoir-response predictions. Considering the non-Darcy flow in matrix and the stress-sensitive effect, Yan et al. (2024) proposed a new physics-based data-driven surrogate model, i.e. dual-porosity flow-network model. Compared with the full-order model, the production optimization speed of proposed model is increased by more than five times. Machine learning algorithms are reliable tools for building proxy models and reducing simulation costs. Owing to the high cost of combination simulation of WAG injection and fishbone structure producing well, Enab and Ertekin (2021) developed an artificial neural network-based toolbox to evaluate and optimize the operation. Due to the lack of complete production curves and large-scale time series data, machine learning methods may not fully leverage their advantages. Gao et al. (2023) proposed a XGBoost-PSO model to optimize injection and production parameters of CO_2-EOR design. Meng et al. (2024) proposed a new workflow for forming a high-fidelity proxy model dedicated to CO_2-EOR in low permeability reservoirs. The above two types of methods can reduce the design cost of oilfield development scheme and increase production. The optimal solution can be finally given. However, it cannot reveal the relationship between injection and production parameters and objective function.

There are still many studies focusing on the analysis of the influence laws based on physical simulation. The first issue is the selection of injection fluid and mode. Unclear understanding of the mechanism of water-sensitive damage will lead to difficulties in selecting the injection water. Thus, Wang et al. (2019) conducted oil displacement experiment with different water salinities. Then, a productivity equation considering low-velocity nonlinear flow and stress sensitivity was established to evaluate the impact of reservoir property changes. Water quality restricts effective implementation of water injection in low permeability reservoirs. Through core experiments, Xiong et al. (2018) quantify the damage to reservoirs caused by particle size and concentration of suspended solids in injected water. To effectively avoid damage to water-sensitive formations, CO_2 flooding is an effective way that can also increase recovery and store CO_2 (Wang et al., 2025b). However, its performance is often damaged by the gas channeling due to reservoir heterogeneity (Zhang et al., 2024). Through core flooding experiments, Li et al. (2018) evaluated four CO_2 injection schemes in low permeability cores. They found that the smaller injection rate contributes to the delay of CO_2 breakthrough and reaches a higher oil recovery. Emami-Meybodi et al. (2024) reviewed the cyclic gas injection modeling and experiments in low-permeability oil reservoirs. They reported that water alter gas injection can delay the gas channeling and achieve balanced development. The aforementioned studies experimentally evaluated the selection of injection fluids.

To provide more guidance on injection rate/timing for oilfield development, some indoor experiments were carried out. For WAG injection and the intermittent gas (IG) injection, Wang et al.

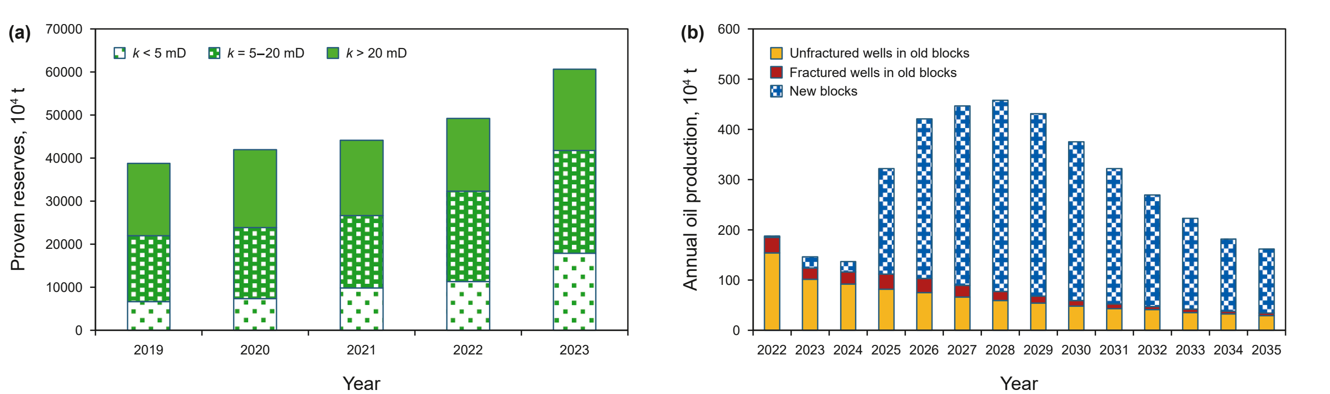

Fig. 1. **(a)** Proven geological reserves of crude oil in offshore low-permeability sandstone reservoirs. **(b)** Prediction of production profile for offshore low-permeability reservoirs.

(2022) studied the comparison and the injection parameters in ultra-low permeability reservoir. They reported that the economic IG flooding round is 7. The optimized IG flooding period after gas breakthrough is 6 h. Wang et al. (2018) obtained the key factors affecting the imbibition effect of low permeability core through experiments. Then they established an imbibition's rate expression for reservoir simulation. For extra-low permeability (1–10 mD) cores, Xiao et al. (2017) found that cyclic CO_2 injection displacement in the micro pores has the highest efficiency, followed by CO_2 miscible flooding, WAG flooding and immiscible CO_2 flooding. Qualitative understanding can guide the choice of development methods. However, the quantitative optimized parameters are obtained in laboratory. It is difficult to apply directly to actual oilfield.

To guide the actual oilfield development, the optimal injection pressure is usually analyzed based on field data. Controlling water injection pressure to prevent water breakthrough and floods along natural fractures is an effective measure for improving the waterflooding development effect. Lyu et al. (2018) proposed an approach for determining the water injection pressure based on the opening pressure of natural fractures in fractured low-permeability reservoirs. Under the condition of synchronous injection and production of horizontal wells, Wang et al. (2020) also determined the limit of water injection pressure to avoid large-scale opening of natural fractures.

Another effective way to guide the actual oilfield development is numerical reservoir simulation. Different geologic characteristics and different physical fluid properties decide different cycle number and WAG ratios, Liu et al. (2016) investigated the gas alternative water (WAG) for CO_2 flooding optimization in Jilin oil fields, China. The optimal parameters are 7 slugs, a total injection volume PV of 0.3845, and a gas-water slug ratio of about 0.5742. Tian et al. (2020) studied gas injection in low permeability reservoirs of Changqing oilfield. They reported that C_3H_8 huff-n-puff achieves the best performance, followed by the produced gas and CH_4. To improve the swept volume of injected gas, oil displacement efficiency, and oil recovery, gas-assisted gravity drainage (GAGD) technology has great potential. Wang et al. (2024) analyzed CO_2 injection schedule for two multi-fractured horizontal wells. Li et al. (2024) studied the oil displacement mechanism in the combination mode of vertical well and horizontal well. They revealed the difference of EOR mechanism between asynchronous and inter-fracture. The above-mentioned various energy supplementation methods are usually targeted at specific reservoirs. It is difficult to guide parameter design under different reservoir properties. Therefore, Zhao et al. (2015) established recommended chart for advanced water injection intensity in ultra-low permeable-tight oil. They also reported that the timing of advanced water injection should follow the completion of the horizontal wells. However, few studies have examined the impact of low permeability reservoir characteristics on optimization design.

During the injection of CO_2 and water, many researchers have used geochemical reaction methods to study dissolution and rock-water interactions (Behera et al., 2024). Alhosani and Daraboina (2021) developed an integrated multiphase simulator by coupling thermodynamics, hydrodynamics, heat transfer, and asphaltene modules, validating it with field data to predict asphaltene deposition and analyze multi-phase flow impacts. Jin et al. (2016) modeled geochemical reactions during CO_2 injection in saline aquifers, assessing formation damage risk from mineral dissolution/precipitation and its effect on injectivity. Khurshid and Afgan (2021) investigated water composition's impact on formation damage and energy recovery in geothermal reservoirs via geochemical simulations, focusing on scale precipitation and geomechanical effects of porosity/permeability changes. Asaadian et al. (2022) explored acid-induced sludge formation's impact on rock wettability and permeability. Khurshid et al. (2022) developed a 1D radial numerical model coupling fluid flow, asphaltene deposition, and acid-asphaltene reactions to investigate sludge formation's effect on worm holing during carbonate acidizing.

In summary, fracture injection optimization assisted by intelligent optimization algorithm is difficult to reveal the influence of engineering parameters on production dynamics. Existing studies on finding inflection points based on sensitivity analysis are mostly aimed at a specific target reservoir and are difficult to guide new reservoir blocks. Existing research has not yet studied the impact of complex flow mechanisms on optimization results. Existing embedded discrete fracture model (EDFM) that consider low-velocity nonlinear flow and stress sensitivity are usually based on black oil model, which are difficult to use to analyze the effects of gas injection parameters.

In this paper, we first established a compositional reservoir simulation method based on 3D-EDFM. Multiple characteristics of offshore low permeability oil reservoir are taken into account. Then we conducted the injection fluid selection. In the optimization process, the injection rate and timing under CO_2 and H_2O flooding conditions are investigated sequentially with staggered well pattern. To effectively guide new reservoir blocks, the influence of different matrix permeability on the optimization results was investigated. Furthermore, the effect of the low-velocity nonlinear flow on the optimal parameters was studied.

2. Methods

In this paper, the basic 3D-EDFM is adopted from the MRST. It is an open-source framework for rapid prototyping and evaluation of reservoir simulation problems. The low-velocity nonlinear flow, matrix and fracture stress sensitivity equations are adopted from our previous work. Then the corresponding matrix and fracture grid nonlinear transmissibility is proposed to solve the multi-component, multi-mechanism flow equations. The cumulative oil production at a certain water cut/gas oil ratio is applied as the objective function.

2.1. Fluid flow in low permeability oil reservoir

The multi-phase multi-component fluid flow in the matrix and hydraulic fractures satisfies the mass conservation (Jiang et al., 2025) and diffusion equation (Rui et al., 2025). As shown in Eq. (1).

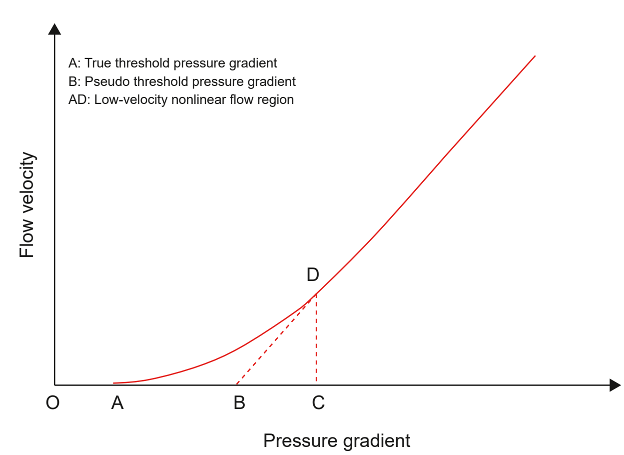

Fig. 2. Schematic diagram of low-velocity nonlinear flow.

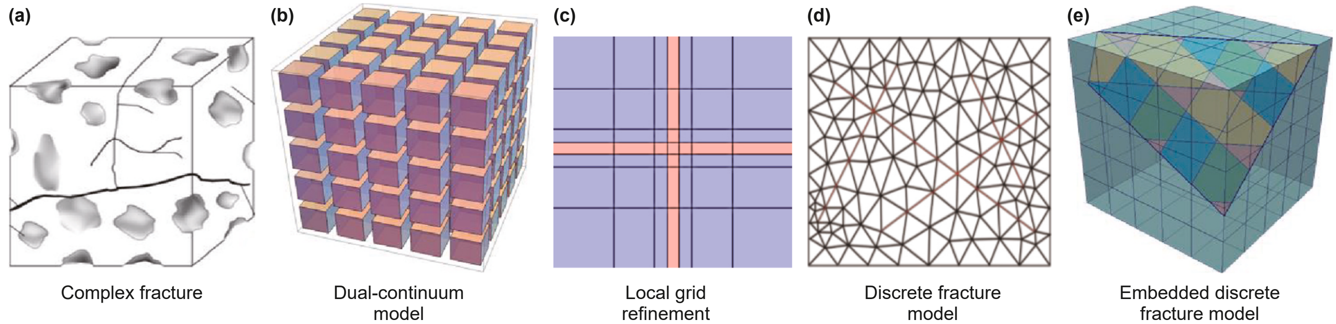

Fig. 3. Fracture characterization methods comparison: **(a)** actual complex fracture, **(b)** dual-continuum model, **(c)** local grid refinement (LGR), **(d)** discrete fracture model (DFM), **(d)** embedded discrete fracture model.

Table 1
Comparison of different method.

Model	Dual-continuum model	Local grid refinement	Discrete racture model	Embedded discrete fracture model
Accuracy	×	✓	✓	✓
Flexibility	×	×	✓	✓
Gridding	✓	✓	×	✓
Computational efficiency	✓	×	×	✓

Note: ✓ represents good, available or supported, while × denotes poor, not available or not supported.

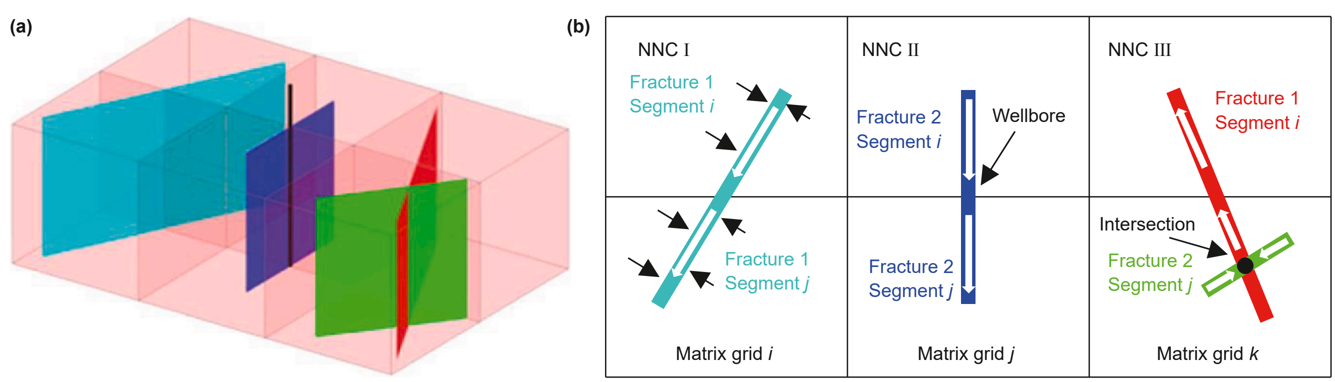

Fig. 4. **(a)** Physical model of the fractured reservoir, **(b)** EDFM mesh.

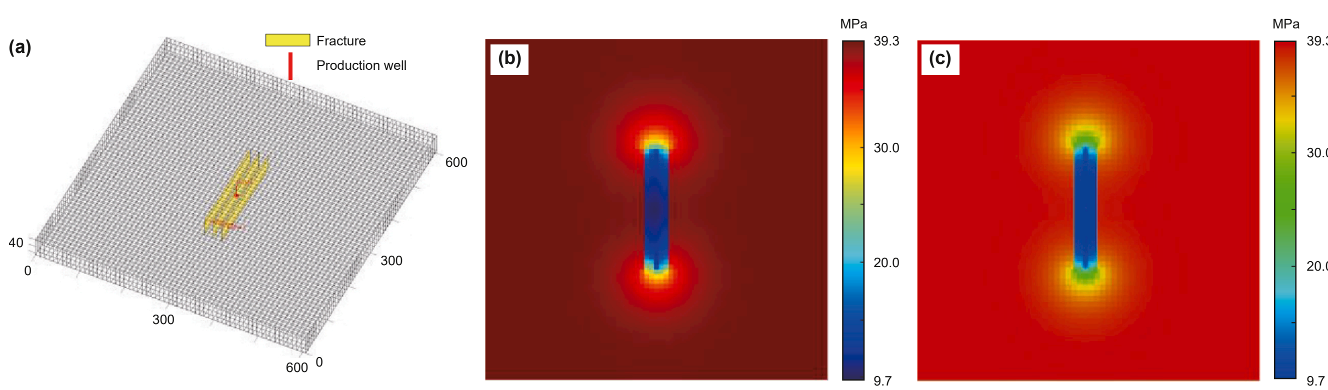

Fig. 5. Physical model **(a)** and pressure field comparison after one month production between EDFM **(b)** and CMG-GEM **(c)**.

$$\left(\sum_j \rho_j \omega_{ij} \vec{v}_j + \sum_j J_{i,j}\right) + q_i = 0, \;\; i = 1, ..., n_c; \;\; j = o, g \tag{1}$$

The diffusion is described by Fick's law.

$$J_{i,j} = -\phi \rho_j S_j D_{ij} \nabla \omega_{ij}, \;\; i = 1, ..., n_c; \;\; j = o, g \tag{2}$$

In low-permeability oil reservoir, microscale pore throats are widely distributed. The interaction between fluids and solids is

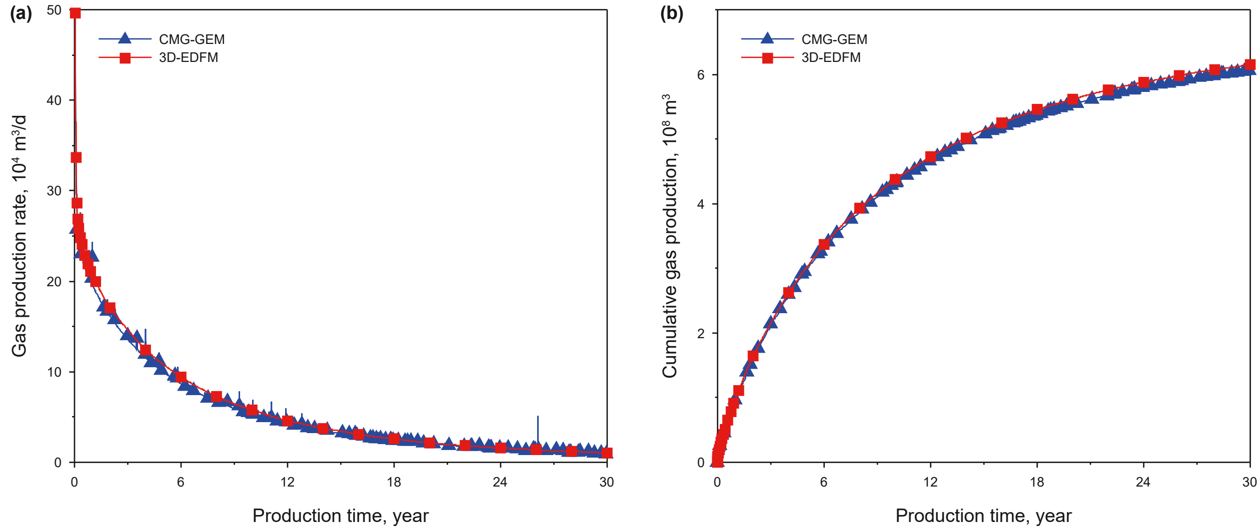

Fig. 6. The comparison of gas production rate (**a**) and cumulative gas production (**b**) between EDFM and CMG-GEM.

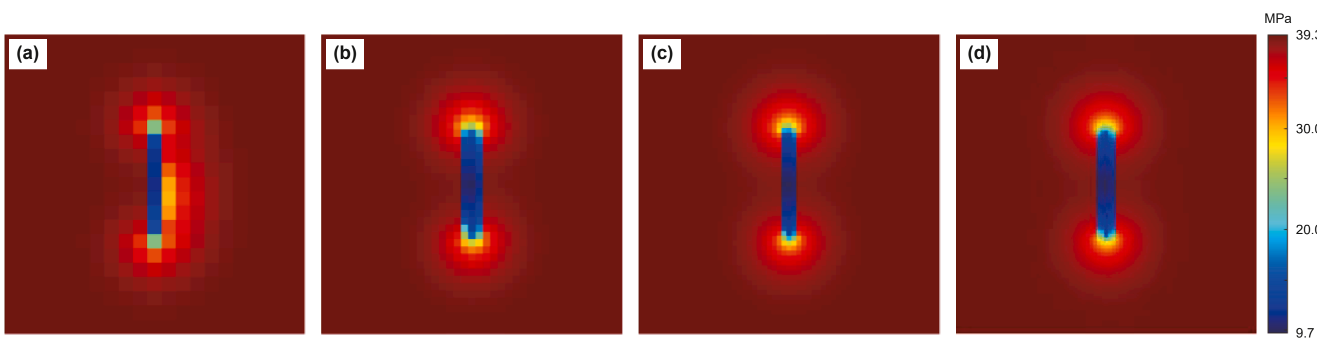

Fig. 7. The pressure field comparison of different mesh size. (**a**) 30 m, (**b**) 15 m, (**c**) 10 m, (**d**) 7.5 m.

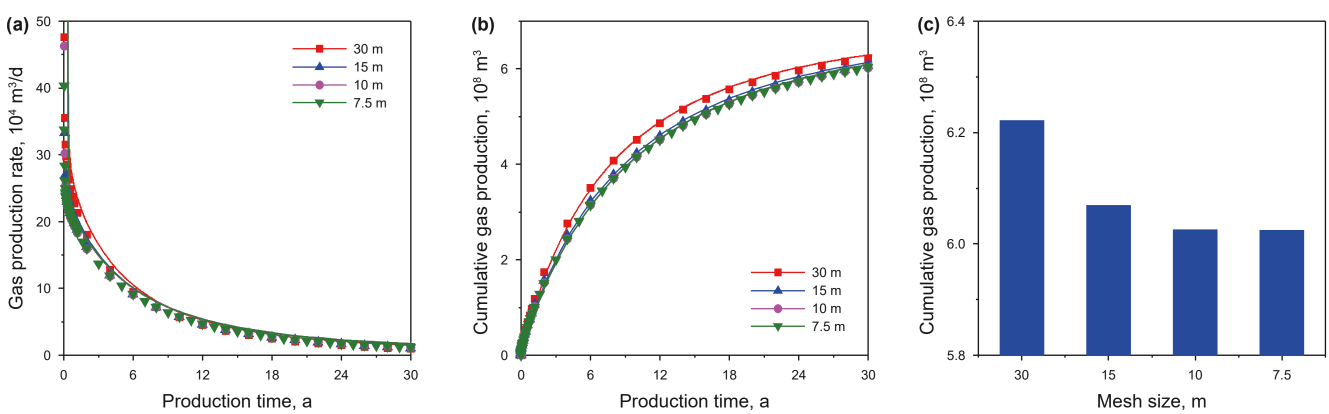

Fig. 8. The comparison of performance between different mesh size. (**a**) Gas production rate, (**b**) cumulative gas production, (**c**) final cumulative gas production.

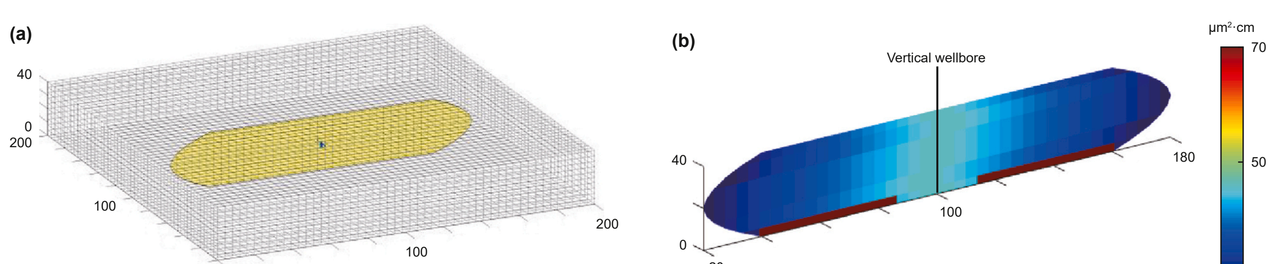

Fig. 9. (**a**) Elliptical hydraulic fracture. (**b**) Initial fracture conductivity distribution.

Table 2
The properties of each pseudo-component.

Pseudo-component	T_c, °R	P_c, psi	m_w, g/mol	Acentric factor	V_c, m^3/mol	Parachor
CO_2	547.56	1069.86	44.01	0.225	9.4×10^{-5}	78
N_2	227.16	492.31	28.01	0.04	8.95×10^{-5}	41
C_1	343.08	667.19	16.04	0.008	9.9×10^{-5}	77
C_2-C_5	494.53	536.40	52.02	0.1723	2.29×10^{-4}	171.07
C_6-C_{10}	789.62	368.57	103.01	0.2839	3.94×10^{-4}	297.42
C_{11+}	1332.52	257.91	267.15	0.6716	8.87×10^{-4}	661.45

Table 3
Binary interaction parameters for oil components.

Component	CO_2	N_2	C_1	C_2–C_5	C_6–C_{10}	C_{11+}
CO_2	0	0.02	0.103	0.1299	0.15	0.15
N_2	0.02	0	0.031	0.082	0.12	0.12
C_1	0.103	0.031	0	0.0174	0.0462	0.111
C_2–C_5	0.1299	0.082	0.0174	0	0.0073	0.0444
C_6–C_{10}	0.15	0.12	0.0462	0.073	0	0.0162
C_{11+}	0.15	0.12	0.111	0.0444	0.0162	0

strong and cannot be ignored. Some microtube experiments also show that the boundary layer thickness is inversely proportional to the pressure gradient. This leads to the phenomenon of low-velocity nonlinear flow in matrix (Wang et al., 2025a). The schematic diagram of the typical low-velocity nonlinear flow curve used in this work is depicted in Fig. 2 (Song et al., 2019). The fluid in the OA segment does not flow. The fluid in the AD segment flows slowly, and the subsequent segment is a straight line. The value of point A is regarded as true threshold pressure gradient (TPG). Point

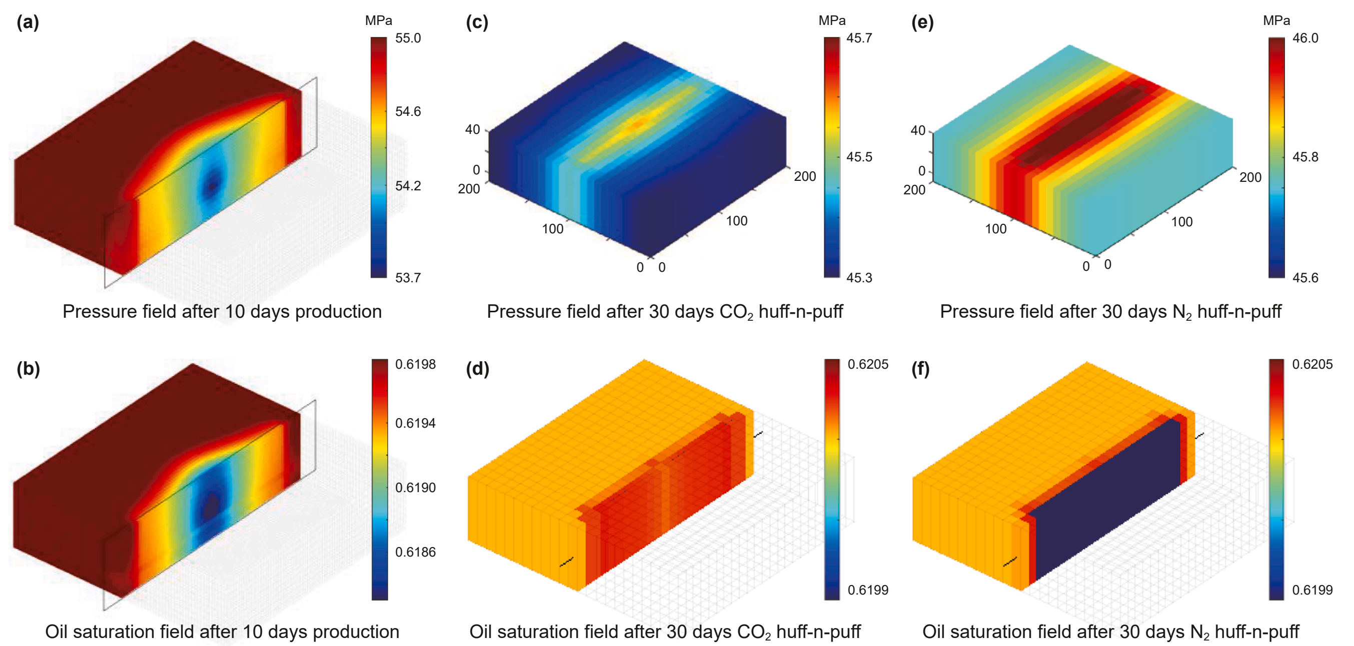

Fig. 10. Field comparison of production and CO_2/N_2 huff-n-puff. The upper row is pressure field. The lower row is the oil saturation field. **(a)**, **(b)** are the field after 10 days production. **(c)**, **(d)** are the field after 30 days CO_2 huff-n-puff. **(e)**, **(f)** are the field after 30 days N_2 huff-n-puff.

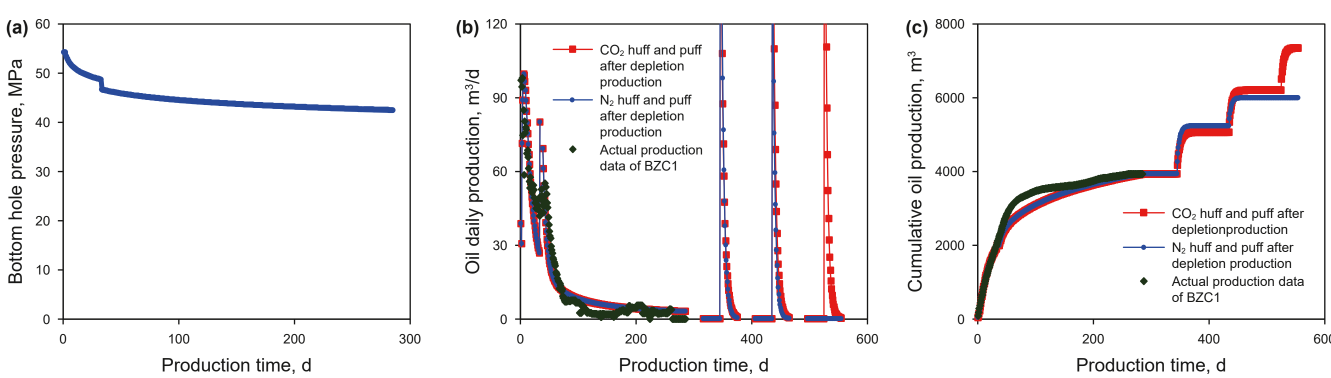

Fig. 11. Comparison of production performance of CO_2/N_2 huff-n-puff after production history matching. **(a)** is the actual bottom hole pressure. **(b)** is the oil daily production performance. **(c)** is the cumulative oil production performance.

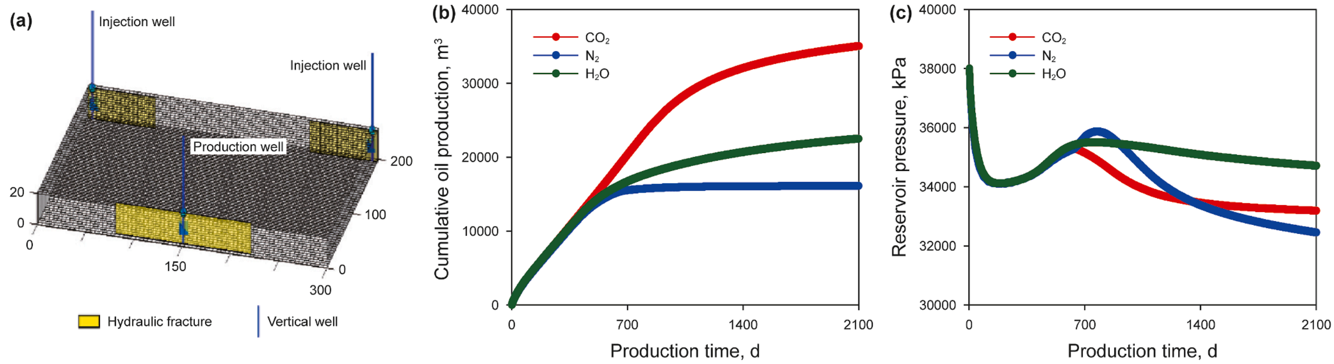

Fig. 12. **(a)** is the staggered well pattern. **(b)** **(c)** are the cumulative oil production and reservoir pressure comparison between different injection fluid.

Table 4
Cumulative oil production comparison between different injection fluid.

Injection fluid	Cumulative oil production, $\times$ 10^4 m^3
CO_2	35.16
N_2	0.02
CH_4	0.15

B is the intersection of the reverse extension of the straight-line segment and the x-axis. The value of point B is regarded as the pseudo TPG.

The low-velocity nonlinear flow equation is adopted from our previous work (Xu et al., 2025b).

$$\begin{cases} \boldsymbol{v}_{\kappa,\mathrm{m}} = 0 & \nabla p_{\kappa,\mathrm{m}} < G \\ \boldsymbol{v}_{\kappa,\mathrm{m}} = -\dfrac{k_{\kappa,\mathrm{m}}}{\mu_\kappa}\left(\nabla p_{\kappa,\mathrm{m}} - G\right)\left(1 - \delta_{\mathrm{rD}} - \delta_{\mathrm{iD}} \mathrm{e}^{-c_\varphi(|\nabla p| - G)}\right)^4 & \nabla p_{\kappa,\mathrm{m}} \geq G \end{cases} \tag{3}$$

The matrix stress sensitivity adopts traditional exponential empirical formula as Eq. (4).

$$k_{\mathrm{m}} = k_{\mathrm{mi}} \times \mathrm{e}^{\gamma(p_{\mathrm{m}} - p_{\mathrm{mi}})} \tag{4}$$

Fluid flow in hydraulic fracture follows Darcy flow.

$$\boldsymbol{v}_{\kappa,\mathrm{hf}} = -\frac{k_{\kappa,\mathrm{hf}}}{\mu_\kappa} \nabla p_{\kappa,\mathrm{hf}} \tag{5}$$

To consider fracture stress sensitivity characteristics, the conductivity attenuation model is used from our previous work (Xu et al., 2025b).

$$F_{\mathrm{c}} = F_{\mathrm{ci}}\left(\eta_{\mathrm{i}} \mathrm{e}^{-C(\sigma_{\mathrm{h}} - p)} + \eta_{\mathrm{r}}\right) \tag{6}$$

In addition, some other constraints are listed as follows.

$$\begin{aligned} & S_{\mathrm{o}} + S_{\mathrm{g}} + S_{\mathrm{w}} = 1 \\ & \sum_{i=1}^{N_{\mathrm{c}}} x_i = 1 \ \sum_{i=1}^{N_{\mathrm{c}}} y_i = 1 \ \sum_{i=1}^{N_{\mathrm{c}}} z_i = 1 \end{aligned} \tag{7}$$

The oil and gas properties are calculated based on the vapor–liquid equilibrium (VLE) calculation. VLE calculation includes phase stability test and flash calculation. The traditional Peaceman-type well model is adopted to control well schedule.

2.2. Meshing and model solving based on EDFM

Fig. 3 shows different method for dealing with complex fractures. The advantages and disadvantages are listed in Table 1. Compared to dual-continuum, local grid refinement and discrete

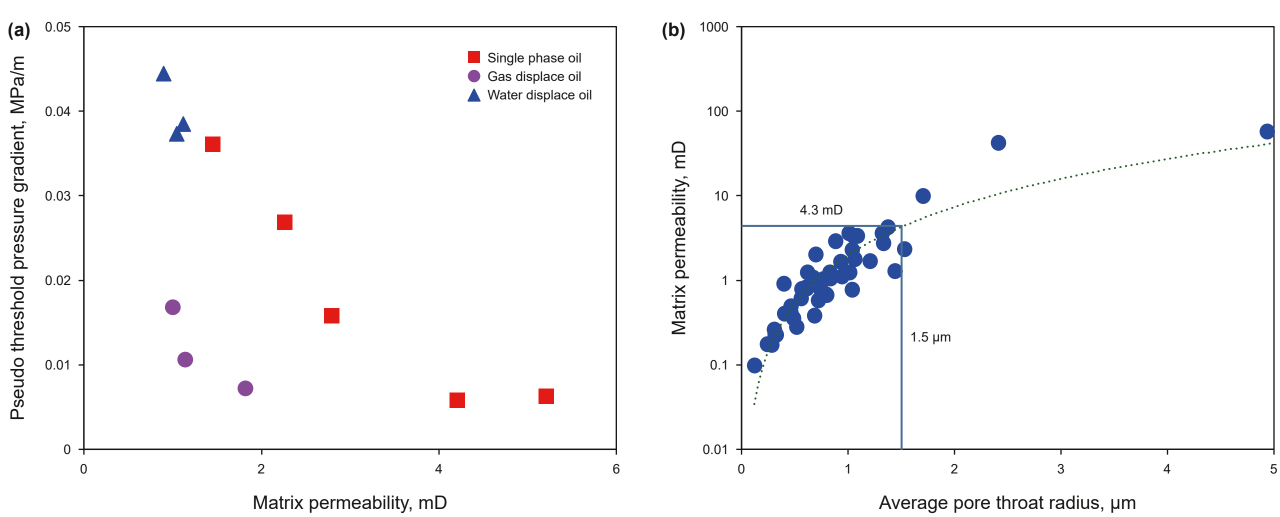

Fig. 13. **(a)** The pseudo threshold pressure gradient under different fluid media measured by core flooding experiment. **(b)** Relationship between matrix permeability and average pore throat radius in target reservoir.

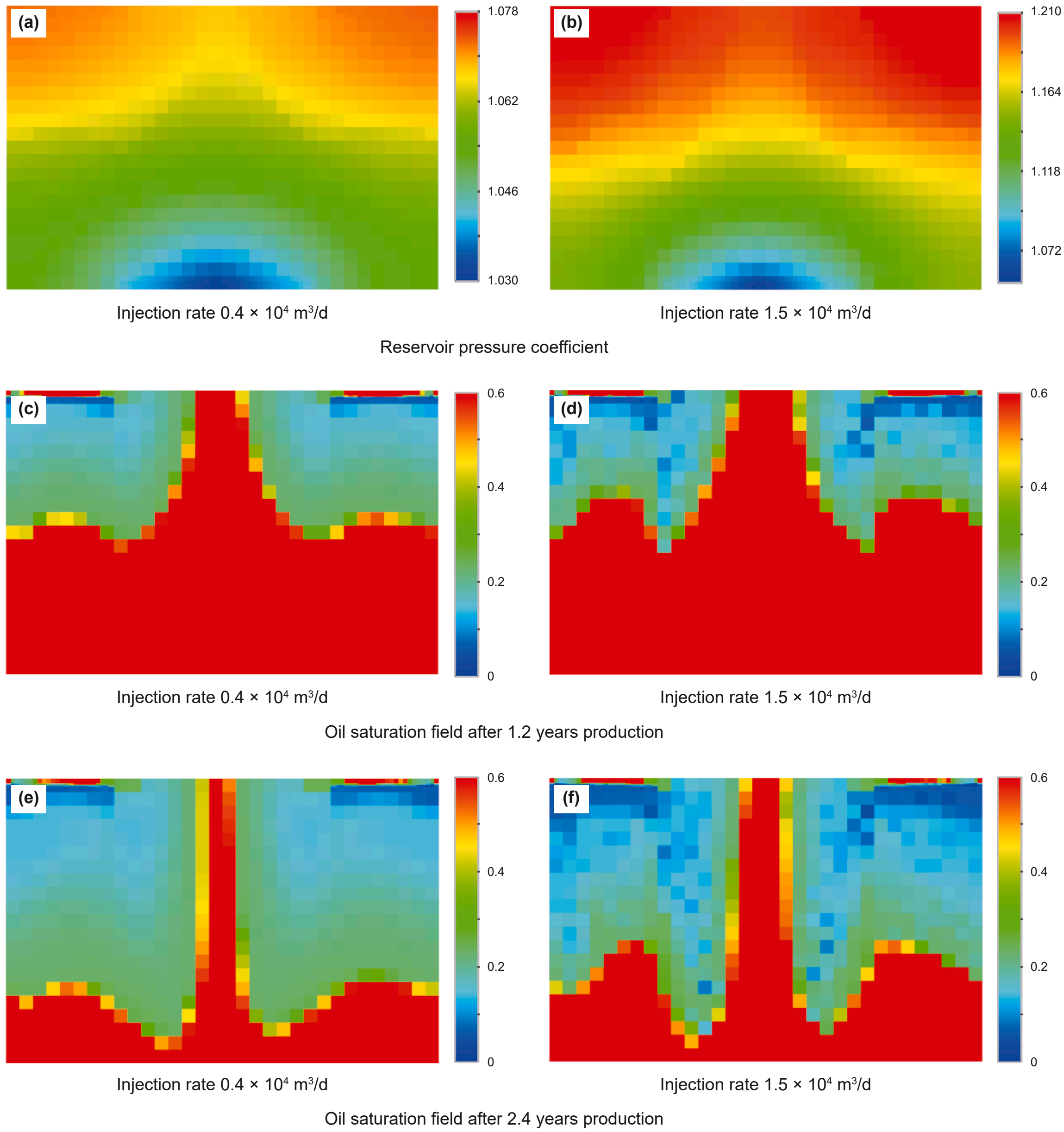

Fig. 14. **(a)** **(b)** are the reservoir pressure coefficient under different injection rate. **(c)** **(d)** are the oil saturation field after 1.2 years production. **(e)** **(f)** are the oil saturation field after 2.4 years production.

fracture models, EDFM can provide similar accuracy to DFM by explicitly embedding each fracture as a lower-dimensional object within a simple matrix grid. It avoids the meshing burden of LGR or DFM and flow error in dual continuous media. The workload of mesh generation is significantly reduced to the level of basic structured meshes. This non-embedded approach grants unlimited flexibility in orientation and network complexity. Thus, EDFM is very suitable for fracture parameter optimization in heterogeneous reservoirs. EDFM keeps computational cost near the dual-continuum level while preserving high-resolution fracture physics. The other three methods cannot simultaneously achieve a balance between accuracy, flexibility, and mesh generation efficiency.

The EDFM meshing method is applied here (Feng et al., 2020). As shown in Fig. 4, fractures are added to the reservoir in a non-invasive way. This technique treats both the matrix and fracture grids as cells. When a fracture penetrates some matrix cells, the fracture is divided into segments (fracture cells) by the matrix cell boundaries. Then the non-neighboring connections (NNCs) are defined to permit fluid transport between physically linked cells (Xu et al., 2022). Fig. 4 describes three types of NNCs, i.e. fracture–matrix connection, fracture–fracture connection in a same fracture, and fracture–fracture connection between different intersecting fractures. The total transmissibility can be calculated from half transmissibility as Eq. (8) (Lie et al., 2012; Bao et al., 2017).

$$T_{i,j} = \frac{2T_iT_j}{T_i + T_j} \tag{8}$$

where half transmissibility T_i is related with cell permeability k_i, contact area A_i, and vertical distance from center point to contact surface d_i. As shown in Eq (9).

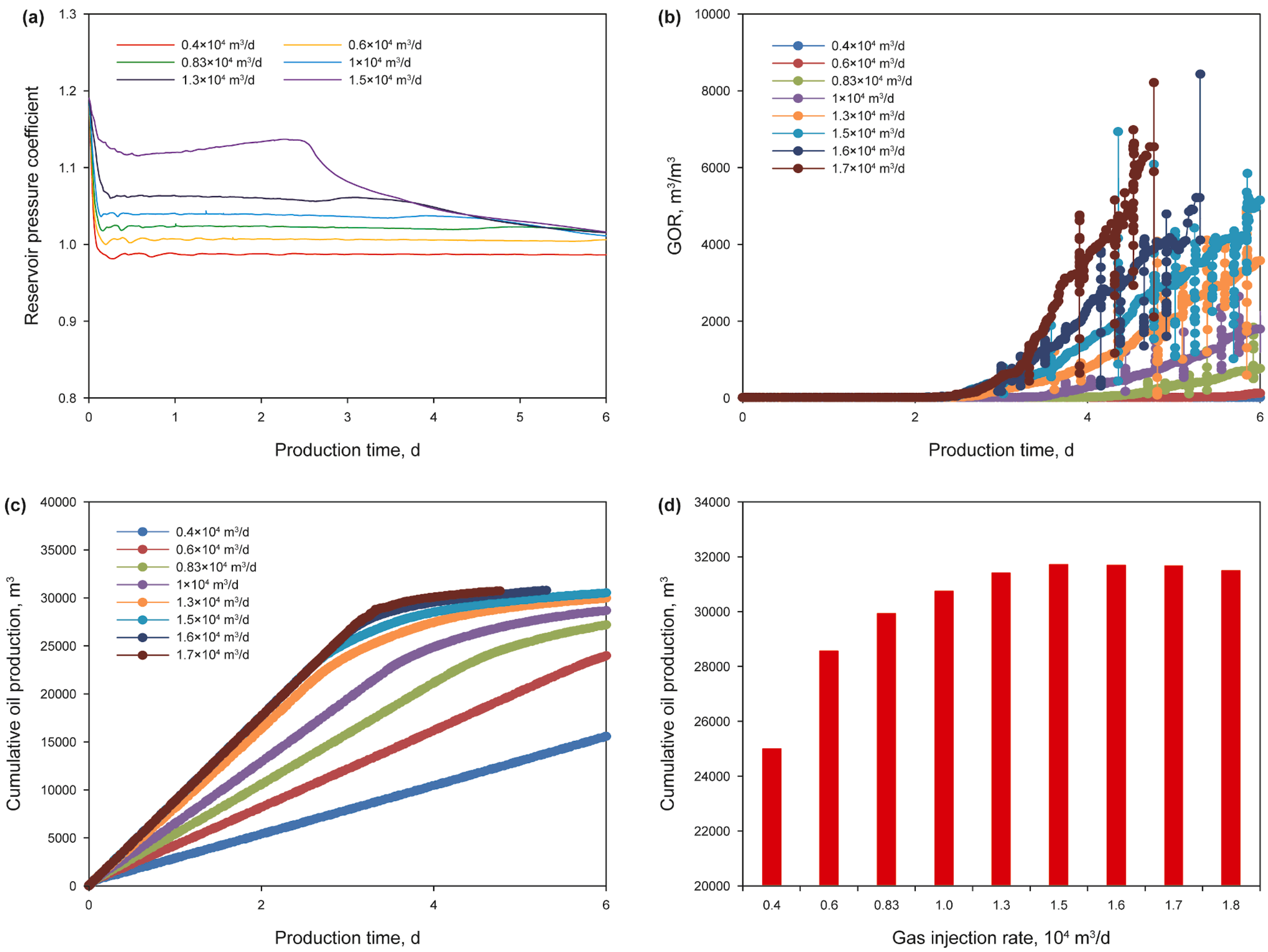

Fig. 15. **(a)** is the reservoir pressure coefficient. **(b)** is the dynamic curve of gas oil ratio. **(c)** **(d)** are the dynamic curve and value of cumulative oil production.

Table 5
Cumulative oil production comparison between different CO_2 injection rate.

Injection rate, $\times$ 10^4 m^3/d	0.4	0.6	0.83	1	1.3	1.5	1.6	1.7	1.8
Cumulative oil production, $\times$ 10^4 m^3	2.50	2.86	2.99	3.07	3.14	3.171	3.17	3.168	3.15

$$T_i = \frac{k_i A_i}{d_i} \tag{9}$$

To consider low velocity nonlinear flow and stress sensitivity in matrix, the half-transmissibility of matrix cell is modified as Eq. (10).

$$\begin{aligned} &T_{mi}{}' = 0 \quad \nabla p_m < G \\ &T_{mi}{}' = T_{mi} \times \left(1 - \delta_{rD} - \delta_{iD} e^{-c_\varphi(|\nabla p_m| - G)}\right)^4 \times e^{\gamma(p_m - p_{m0})} \quad \nabla p_m \geq G \end{aligned} \tag{10}$$

To consider fracture stress sensitivity, the half-transmissibility of fracture cell is revised as Eq. (11).

$$T_{fi}{}' = T_{fi} \times \left(\eta_i e^{-C(\sigma_h - p)} + \eta_r\right) \tag{11}$$

The discretization of the multi-phase multi-component flow equation adopts finite volume method. In each time step, the Jacobian matrix is assembled by automatic differentiation. Then, the nonlinear equations are iteratively solved using the Newton iteration method. More details can be found in our previous work (Ren et al., 2018; Xu et al., 2021).

2.3. Model validation and mesh sensitivity analysis

A compositional model is built using our 3D-EDFM and commercial compositional simulator (CMG-GEM), respectively. The physical model is shown in Fig. 5(a). The reservoir size is 600 m $\times$ 600 m $\times$ 45.7 m. A single hydraulically fractured well in the middle of two sealing barriers, which are basically two vertical fractures with very low fracture conductivity values. The matrix porosity is 0.16. The matrix permeability is 0.1×10^{-3} μm^2. Fracture aperture is 3 mm. Fracture permeability is 50 μm^2. The half-length is 107 m. The sealing barriers permeability is 1×10^{-9} μm^2. A three-component mixture of methane (C_1), ethane (C_2), and propane (C_3) at mole fractions of 0.991, 0.0088, and 0.0002, respectively, is adopted. The binary

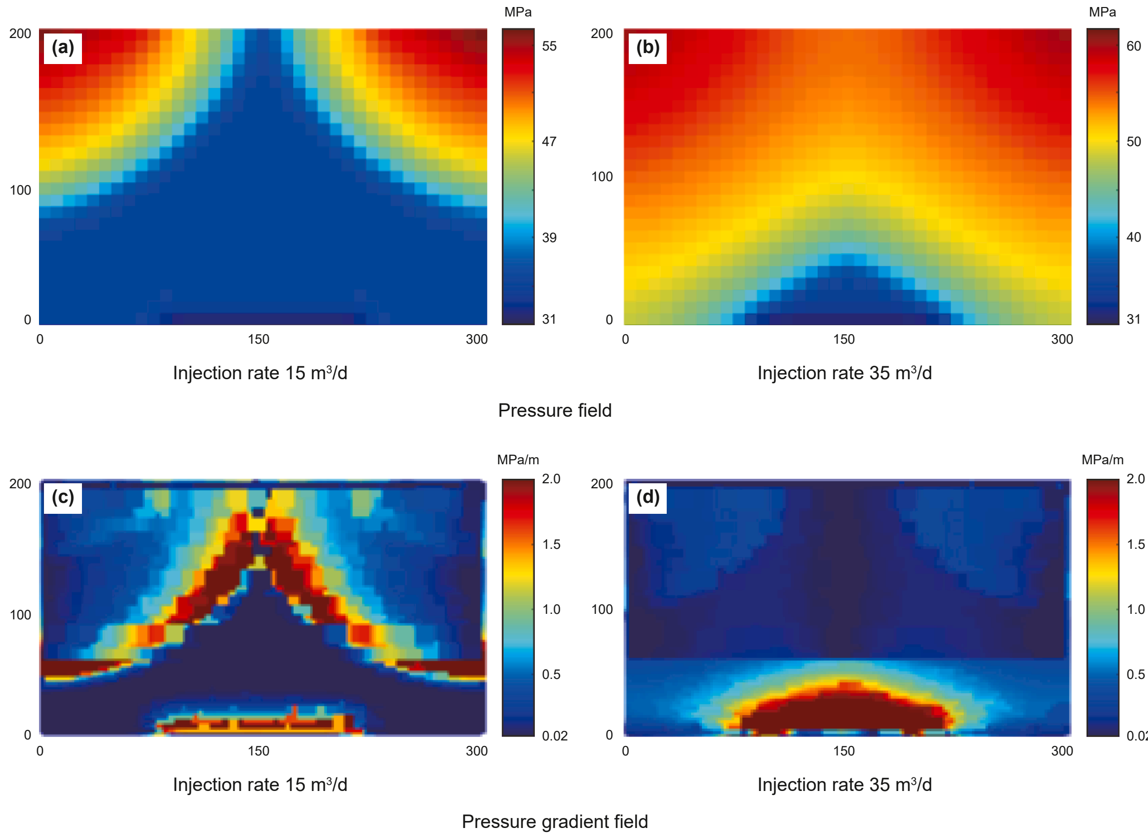

Fig. 16. Pressure **(a, b)** and pressure gradient **(c, d)** field comparison after 300 days development.

interaction matrix includes mat (1, 2) = 0.005, mat (1, 3) = 0.01, mat (2, 3) = 0.005. Initial reservoir pressure is 39.3 MPa. Well bottom hole pressure is set as 9.7 MPa. After one month production. The pressure fields are drawn in Fig. 5(b) and (c). The sealing barrier has a significant impact on pressure field. Fig. 6 compares the gas production rate and cumulative gas production between EDFM and CMG-GEM. The gas production performance of our 3D-EDFM matches well with commercial reservoir simulator.

Furthermore, the mesh sensitivity analysis is conducted based on the validation case. The matrix grid size is changed to evaluate the pressure field and production performance. As shown in Fig. 7, when the mesh size is 30 m, the pressure field exhibited some oscillations. As the mesh size decreases, the pressure field becomes more stable. Fig. 8(a) compares the gas production rate of different mesh size. A larger grid size primarily affects the initial daily gas production. As shown in Fig. 8(b) and (c), as the mesh size increases, the cumulative gas production gradually decreases and tends to stabilize. The calculation error gradually decreases, but the computational cost gradually increases. Therefore, the recommended mesh size is 10 m.

2.4. Field application of the 3D EDFM

The 3D EDFM is first applied to history matching and prediction of a fractured vertical well, BZC1. Reservoir model size within the control area of a single well is set as 200 m × 200 m. Reservoir thickness is 40 m. Both the horizontal and vertical grid size are 4 m. The upper and lower layers limit the fracture height to 40 m. As shown in Fig. 9(a), the hydraulic fracture tips are considered to be elliptical. At present, guar fracturing fluid is usually used in offshore fracturing. Due to high viscosity of the fracturing fluid, the proppants settle slowly and have a long suspension time. After the fracture is closed, the height of the sand bank formed at the bottom of the fracture is small. Thus, the initial fracture conductivity distribution is shown in Fig. 9(b). The sand bank at the bottom of the fracture has the highest conductivity. In the suspended proppant part, the initial fracture conductivity gradually decreases from the wellbore to the fracture tip.

There are 6 pseudo-components in the BZC1 model. As shown in Table 2, the properties of each pseudo-component including critical temperature (T_c), critical pressure (P_c), molar weight (m_w), acentric factor, critical volume (V_c), and Parachor coefficient. Initial mole fraction is sequentially set as 0.01183, 0.00161, 0.11541, 0.26438, 0.38089, 0.22588. The binary interaction parameters between each pseudo-component are listed in Table 3. In this way, the fluid properties are calculated using the Peng-Robinson EOS and flash calculations.

Fig. 10 depicts different field comparison of production and CO_2/N_2 injection stages. In the production stage, due to the fracture conductivity distribution, both the pressure (Fig. 10(a)) and oil saturation (Fig. 10(b)) near the wellbore are lower than those around the fracture tip. In the gas huff-n-puff stage, due to the dissolution and diffusion of CO_2, CO_2 can flow farther than N_2. Therefore, after CO_2 injection, the pressure around hydraulic fracture is lower than that N_2 injection (Fig. 10(c) and (e)). For the oil saturation comparison, N_2 will push oil away from fracture. Thus, the oil saturation is lower around hydraulic fracture. While CO_2 is more soluble and has a diffusive effect. The oil saturation after CO_2 injection is higher than that after N_2 injection.

As shown in Fig. 11, BZC1 well is first history matched with actual field production data within 285 days. Then CO_2 and N_2

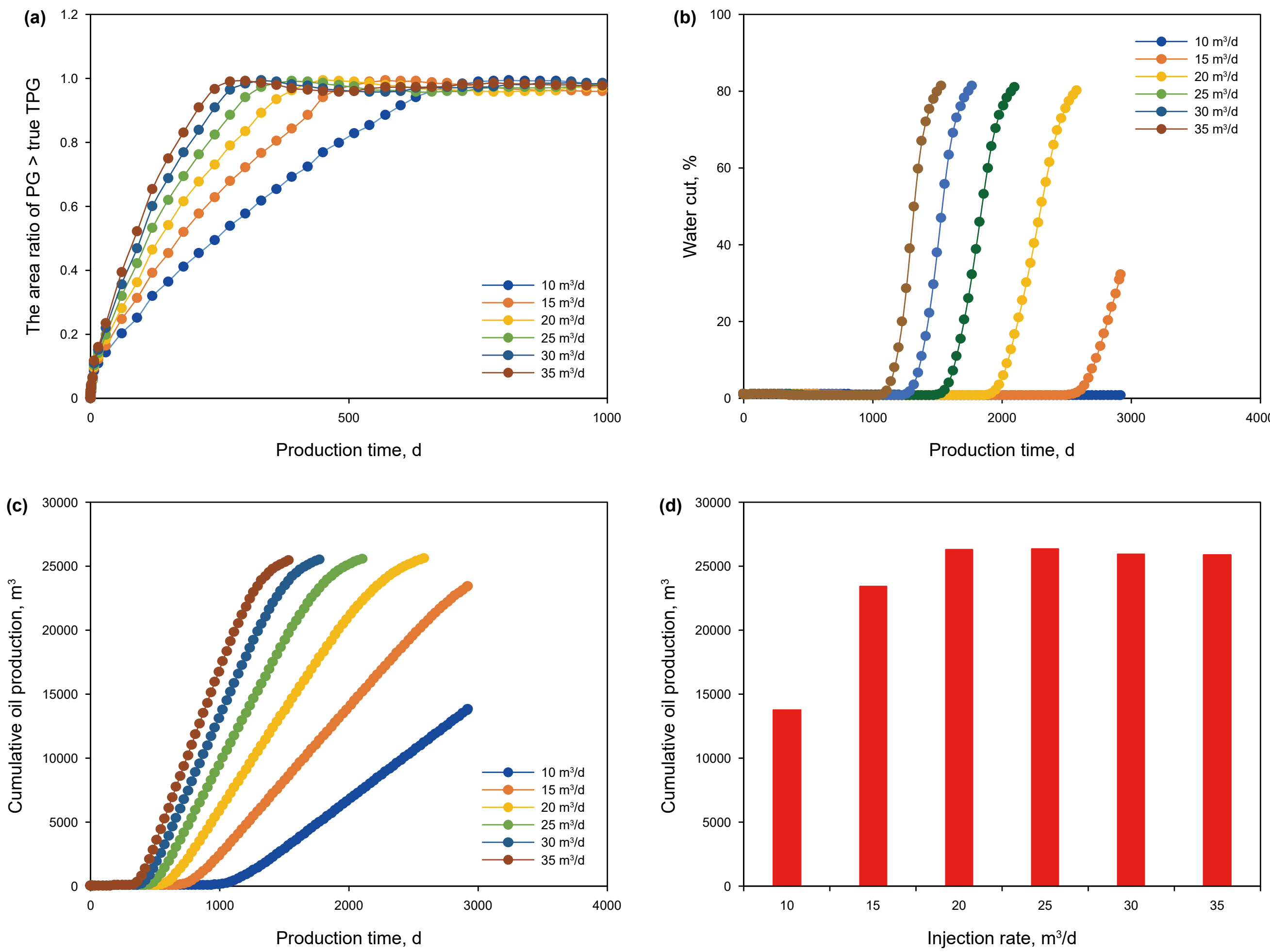

Fig. 17. (**a**) The ratio of the area where the pressure gradient is greater than the true TPG. (**b**) Water cut curve under different injection rates. (**c**) (**d**) are the dynamic curve and value of cumulative oil production.

huff-n-puff are conducted. The actual well bottom hole pressure (BHP) is applied as described in Fig. 11(a). The oil daily production and the cumulative oil production performance are depicted in Fig. 11(b) and (c), respectively. Our simulator matched well with the actual field data. It demonstrated good results in field application. Furthermore, from the perspective of production dynamics, single well depletion production has a rapid decline in production. Therefore, energy needs to be supplemented in the later stage.

In the gas huff-n-puff stage. Both CO_2 and N_2 can significantly increase oil recovery. In the first huff-puff cycle, N_2 increases cumulative oil production by 3.46% compared to CO_2. Because N_2 replenishes more reservoir energy (pressure) than CO_2. In subsequent huff-n-puff cycles, the dissolution and diffusion effects make CO_2 have a wider impact area. The production increase effect of N_2 huff-n-puff is mainly in the first two cycles. While the production increase effect of the third cycle of CO_2 huff-n-puff is still significant. CO_2 increases total cumulative oil production by 22.58% compared to N_2.

2.5. Optimization of injection fluid, rate and timing

Offshore reservoir operation costs are high. The economic benefits of daily oil production at high water cut/gas oil ratio may be difficult to sustain daily costs. Therefore, the objective function J is used cumulative oil production at a certain water cut/gas oil ratio. As shown in Eq. (12).

$$J(\mathbf{u}) = N_\mathrm{p} \quad \text{at} \quad \begin{cases} f_\mathrm{w} = C \\ R_\mathrm{s} = C \end{cases} \tag{12}$$

The optimization variables $\mathbf{u}$ include injection fluid, rate and timing (i.e. start time of injection). The injection fluid includes water, CO_2 and N_2. Injection rate optimization is to solve the problem of whether the reservoir pressure can be reasonably maintained. If the injection rate is high, the water/gas breakthrough will occur earlier, which will lead to a decrease in cumulative oil production. If the injection rate is low, the energy supply to the oil well will be insufficient, which will also lead to a decrease in cumulative oil production. Injection timing is to solve the problem of how high the reservoir pressure should be maintained. If the reservoir pressure is high, the injection capacity of the injection well will be limited, thereby limiting the oil well supply pressure difference. If the reservoir pressure is low, the matrix stress sensitivity is strong, which makes it difficult to supply energy to the oil well. Especially for CO_2 injection, miscibility plays a major role in development. If the reservoir pressure is low, the CO_2 miscibility is low, which will reduce the displacement efficiency.

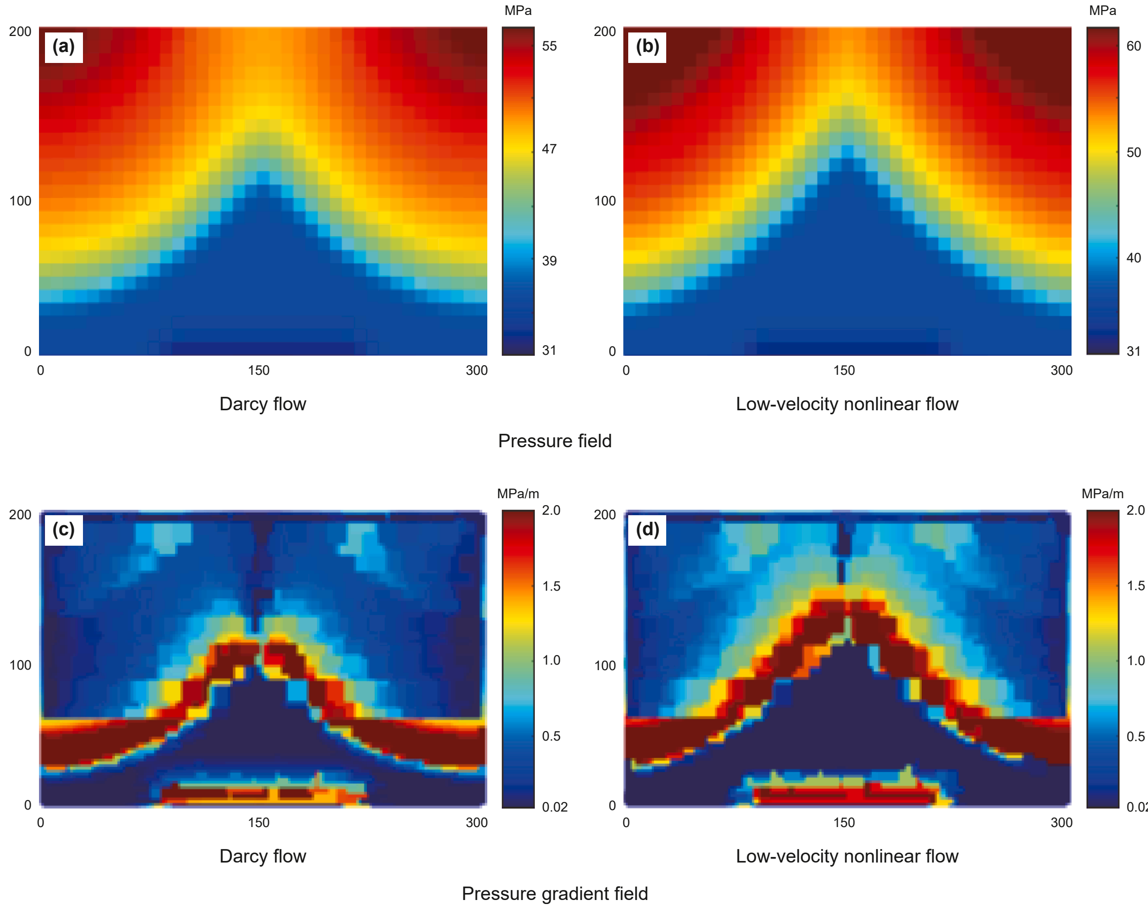

Fig. 18. Comparison between darcy flow (**a**, **c**) and low-velocity nonlinear flow (**b**, **d**) under 20 m^3/d injection rate after 300 days production. (**a**) and (**b**) are the pressure field. (**c**) and (**d**) are the pressure gradient field.

To ensure that the optimization problem is close to the actual field situation (Liu et al., 2018), the upper and lower limit constraints are utilized. As listed in Eq. (13):

$$\text{s.t.}\;\; x_i^{\min} \le \mathbf{u}_i \le x_i^{\max} \left(\mathbf{u}_i = q_{\text{inj}}, t_{\text{inj}}\right) \tag{13}$$

3. Results and discussion

3.1. Injection fluid selection

The staggered well pattern is the most recommended well pattern. It is used as the basic model here (Fig. 12(a)). Model parameters are adopted from the history matching case in Section 2.4. The initial reservoir pressure is 38 MPa. The injection rate under underground conditions is 20 m^3/d. The production well BHP is 30 MPa. As shown in Fig. 12(b), CO_2 flooding increases the cumulative oil production by 35.7% compared to H_2O flooding and by 54.0% compared to N_2 flooding (Table 4). After ~600 days production, the N_2 displacement front reaches the production well and gas channeling occurs. After that, N_2 flooding is unlikely to further increase oil production. Because H_2O has a greater viscosity than N_2, the fingering phenomenon is weaker and the sweep efficiency is larger. Therefore, the development effect of CO_2 is better than N_2. While for CO_2, it has a good dissolution and diffusion mechanism. Thus, CO_2 has a significant effect of increasing energy and reducing viscosity. As shown in Fig. 12(c), before gas breakthrough, the reservoir pressure changes in the same way, due to the same injected fluid volume. After that, the reservoir pressure of N_2 flooding drops fastest, followed by CO_2 and H_2O. From the perspective of development effect and maintaining reservoir pressure, we recommend CO_2 and water as injection fluid.

In actual offshore water and gas injection operations, it is usually necessary to consider the injection capacity and injection water quality. Fig. 13(a) shows the comparison of pseudo TPG measured under different displacement fluids. The displacement methods including single-phase oil flow, gas displacement of oil and water displacement of oil. As the matrix permeability decreases, especially when it is less than 4.2×10^{-3} μm^2, the pseudo TPG of different displacement fluids will gradually increase. The pseudo-TPG variation trend of water displacing or single-phase oil flow is approximate. Furthermore, the pseudo TPG of water-displacing or single-phase oil flow is significantly higher than that of gas-displacing. Fig. 13(b) draws the relationship between matrix permeability and average pore throat radius in target reservoir. As the average pore throat radius increases, the matrix permeability increases significantly first and then increases slowly. According to the target reservoir injection water quality indicators, the median diameter of suspended particles is < 1 μm. According to the 1/3 principle, if the median diameter of the suspended particles is 1 μm, the radius of the pore throat without blockage is 1.5 μm. For our target reservoir, the corresponding matrix permeability is 4.3×10^{-3} μm^2 (Fig. 12(b)). To sum up, for reservoirs with a permeability below 5×10^{-3} μm^2, if the miscible pressure is met, CO_2 flooding is recommended. For reservoirs with a permeability above 5 × 10^{-3} μm^2, water injection is recommended in the early stage, and CO_2 flooding can be switched to further improve the oil recovery.

3.2. Injection rate optimization

3.2.1. Injection rate optimization of CO_2 flooding

Injection rate determines whether the reservoir pressure can be reasonably maintained. CO_2 miscibility is the main factor affecting CO_2 flooding development (Sæle et al., 2022). The staggered well pattern model is used. The matrix permeability is set as 3 × 10^{-3} μm^2. As shown in Fig. 14(a) and b, if the CO_2 injection rate is 0.4 × 10^4 m^3/d, the reservoir pressure coefficient around injection well is ~1.07. While when the CO_2 injection rate increase to 1.5 × 10^4 m^3/d, the reservoir pressure coefficient around injection well will increase to ~1.2. High pressure brings high miscibility. The high miscibility brings the high displacement efficiency. As shown in Fig. 14(c) and (d), after 1.2 years flooding, the oil saturation at an injection rate of 1.5 × 10^4 m^3/d is lower than that at an injection rate of 0.4 × 10^4 m^3/d. However, the injection rate is not the higher the better. The high injection rate will lead to severe gas fingering. As shown in Fig. 14(e) and (f), after 2.4 years injection, the oil saturation distribution shows that the displacement is more uniform when the injection rate is 0.4 × 10^4 m^3/d than when the injection rate is 1.5 × 10^4 m^3/d. Therefore, the sweep efficiency is relatively larger at low injection rate.

To quantitatively evaluate the optimal CO_2 injection rate, the dynamic curves of reservoir pressure, gas oil ratio (GOR), and cumulative oil production are compared in Fig. 15. Before gas breakthrough, high injection rate increases reservoir pressure and improves CO_2 miscibility (Fig. 15(a)). However, it will lead to earlier gas production in production wells and faster GOR increase. When the injection rate is 1 × 10^4 m^3/d, the gas breakthrough time is 3.57 years. When the injection rate is increased to 1.7 × 10^4 m^3/d, the gas breakthrough time is advanced by 31.7%. Meanwhile, the slope of the gas-oil ratio rising curve increased by ~65%. Higher GOR will not be able to meet the high cost of offshore daily operation. Therefore, the objective function uses the cumulative oil production when the gas-oil ratio is 8000 m^3/m^3. The dynamic curve and the final value of cumulative oil production are described in Fig. 15(c) and (d), respectively. The cumulative oil

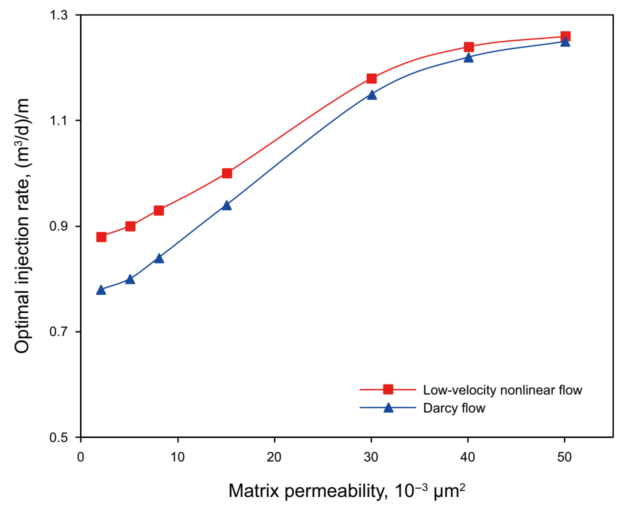

Fig. 20. The optimal injection rate per meter under different matrix permeability with darcy or low-velocity nonlinear flow.

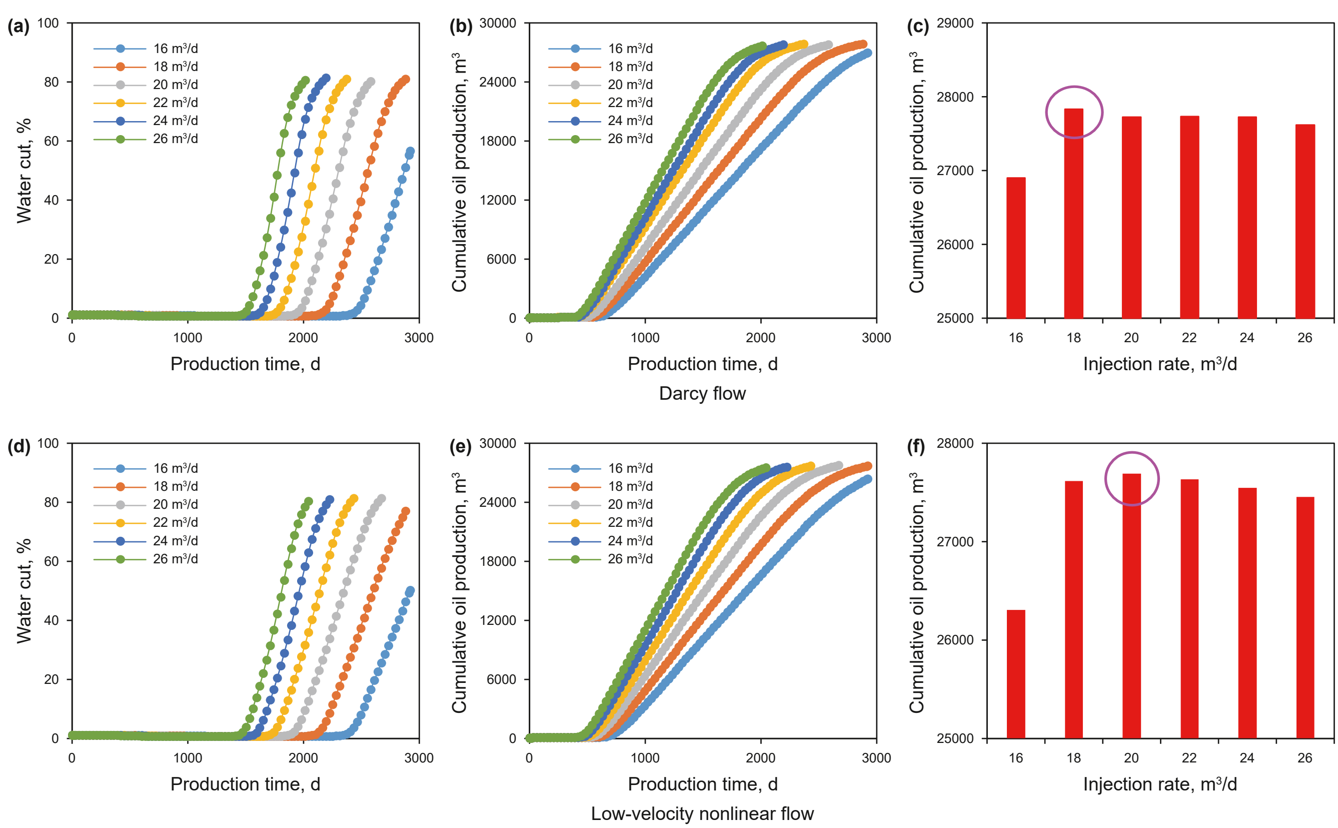

Fig. 19. Water cut and cumulative oil production comparison between the Darcy flow (**(a)**, **(b)** and **(c)**) and the low-velocity nonlinear flow (**(d)**, **(e)** and **(f)**) under different injection rate.

production first increases and then slowly decreases (Table 5). The optimal CO_2 injection rate is 1.5×10^4 m^3/d.

3.2.2. Injection rate optimization of H_2O flooding

The physical model is also shown as Fig. 12(a). The matrix permeability of 15×10^{-3} μm^2 is selected as a typical example. Fig. 16(a) and (b) compared the pressure field under different injection rate after 300 days development. The high-pressure area of 35 m^3/d is larger than that of 15 m^3/d. The corresponding pressure gradient field is depicted in Fig. 16(c) and (d). For the injection rate of 15 m^3/d, the high-pressure gradient area formed at the injection front has not yet reached the production well after 300 days flooding. While for the injection rate of 35 m^3/d, the high-pressure gradient area is concentrated around the production well. The production well is well affected.

To quantitatively evaluate the optimal H_2O injection rate, the dynamic curves of reservoir pressure, water cut, and cumulative oil production are compared in Fig. 17. To quantitatively evaluate the effectiveness of the pressure system, the ratio of the area where the pressure gradient is greater than the true TPG is defined. The larger the ratio, the better the effect of water injection displacement. Fig. 17(a) shows that as time goes by, the ratio gradually increases to 1. It means that the entire injection-production unit achieved effective displacement. Furthermore, as the water injection rate increases, the effective displacement pressure system is established earlier. When the injection rate is 30 m^3/d, the full establishment time is 59% earlier than that of 10 m^3/d. However, the larger the injection rate, the earlier the water breakthrough, and the more serious the ineffective water circulation will be. As shown in Fig. 17(b), the water breakthrough time for 20 m^3/d injection rate is 1950 days. While the water breakthrough time of 30 m^3/d is 1100 days, which is 43.6% earlier. The water cut of 80% is set as the stop condition. Then the dynamic curve and final value of cumulative oil production is draw in Fig. 17(c) and (d), respectively. As the injection rate increases, the production well will be effective earlier. The cumulative oil production will increase faster. However, the critical water cut (80%) will also be reached earlier. Therefore, as the injection rate increases, the cumulative oil production increases significantly first, and then decreases slowly.

We compared the effect of nonlinear flow on injection rate optimization. Fig. 18(a) and (b) compared the pressure field between darcy flow and low-velocity nonlinear flow under 20 m^3/d injection rate after 300 days production. Compared with the Darcy flow, when considering low-velocity nonlinear flow, the fluid flows more slowly under the same pressure difference. Due to the constant injection rate, the pressure field around injection well is higher with low-velocity nonlinear flow (Fig. 18(b)). Fig. 18(c) and (d) compared the pressure gradient field. In Darcy flow, the high-pressure gradient area at the water flooding front advances faster.

The injection rate is selected near the optimal value, i.e. from 16 m^3/d to 26 m^3/d, with an interval of 2 m^3/d. As shown in

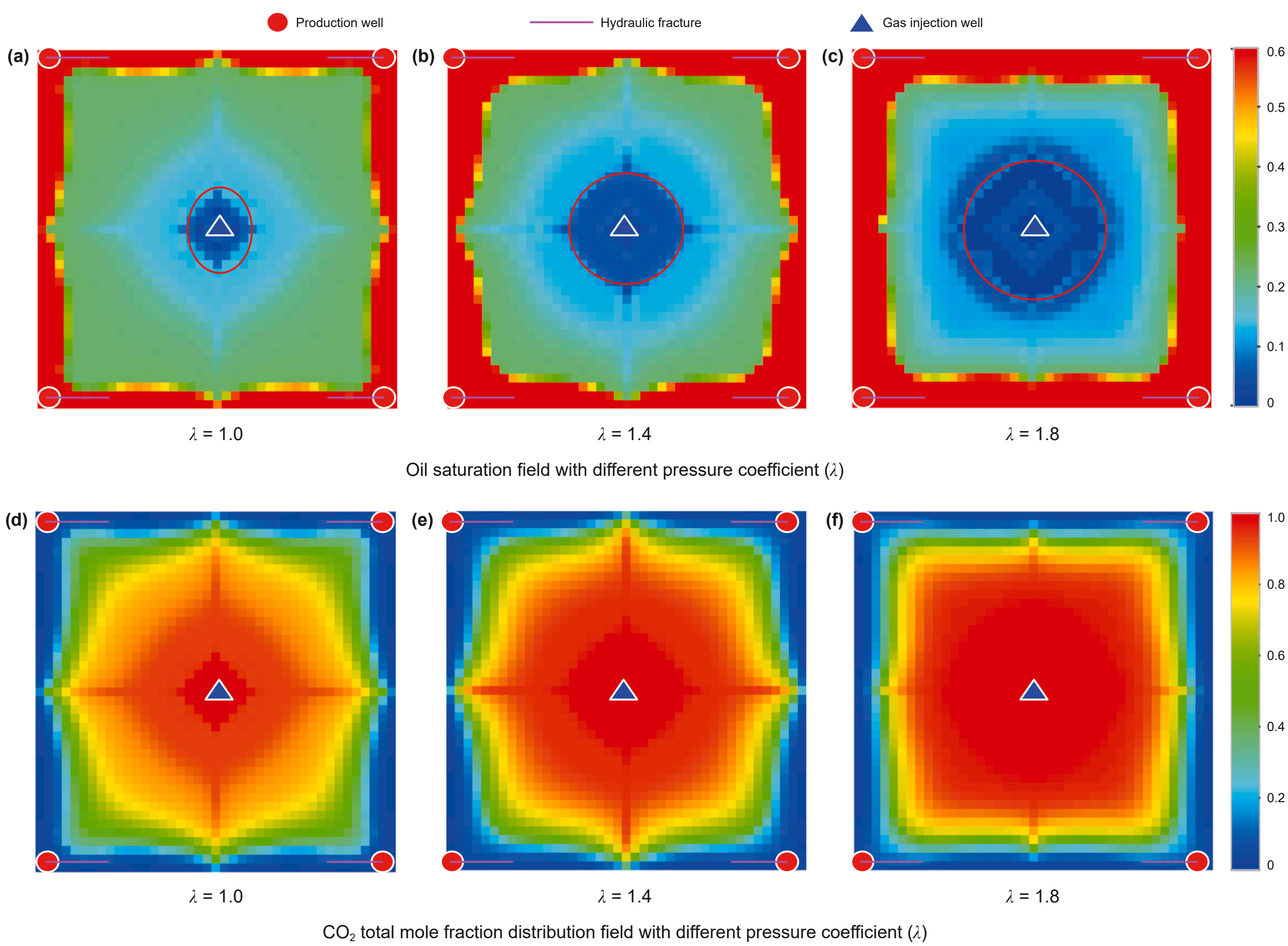

Fig. 21. The oil saturation ((**a**), (**b**) and (**c**)) and CO_2 distribution field ((**a**), (**b**) and (**c**)) with different pressure coefficient.

Fig. 19(a) and (d), with the same injection rate, when low-velocity nonlinear flow is considered, the water breakthrough time is delayed by about 30 days. Because the water flows more slowly. Since the oil flow velocity is also low, the cumulative oil production is reduced by 100–600 m^3. The optimal injection rate for the Darcy flow is 18 m^3/d. While the optimal injection rate for the low-velocity nonlinear flow is 20 m^3/d, representing an 11.1% increase.

To guide new reservoir blocks, the optimization for different matrix permeability model is conducted. The optimal curve is depicted in Fig. 20. As the matrix permeability decreases, the optimal injection rate gradually decreases. The optimal injection rate considering low-velocity nonlinear flow is higher than that with the Darcy flow. The lower the matrix permeability, the more significant the low-velocity nonlinear flow phenomenon is, and the greater the difference in the optimal injection rate is.

3.3. Injection timing optimization

3.3.1. Injection timing optimization of CO_2 flooding

Injection timing determines reservoir pressure. For CO_2 flooding, miscibility plays a more significant role than matrix stress sensitivity. If the reservoir pressure is low, the CO_2 miscibility is low, which will reduce the displacement efficiency. The basic model is adopted from section 3.2.1. The initial reservoir pressure is set 25 MPa. While the minimum miscibility pressure (MMP) is 35 MPa. Since the initial reservoir pressure is lower than the miscible pressure, we inject CO_2 in advance to make the reservoir pressure reach different levels. The pressure coefficient (λ) includes 1.8, 1.5, 1.4, 1.2, 1.0. The entire five-point well group is established. Fig. 21 depicts the oil saturation and total CO_2 mole fraction distribution field with different pressure coefficient after 13.5 years production. As the injection timing is advanced, the reservoir pressure coefficient (λ) gradually increases. As a result, the miscibility of CO_2 and crude oil is higher, the residual oil saturation around the injection well is lower in Fig. 21(c). The area with low residual oil saturation is larger. Meanwhile, the total CO_2 mole fraction is higher (Fig. 21(f)).

Furthermore, we quantitatively evaluate the development effect. Fig. 22(a) shows the cumulative oil production over time. Before gas breakthrough, due to the same injection rate, the growth rate of cumulative oil production is almost the same. However, the gas breakthrough occurs earlier with lower λ. The breakthrough time with $\lambda = 1$ is 12 years, while the breakthrough time with $\lambda = 1.8$ is 14 years. After gas breakthrough, the growth rate of cumulative oil production significant decline. Fig. 22(b) depicts the reservoir pressure coefficient curves. Due to the dissolution and miscibility of CO_2, although the injection and production are balanced, the pressure coefficient gradually decreases. After gas breakthrough, the pressure drops faster. Pressure coefficient is relative to the initial reservoir pressure. Development

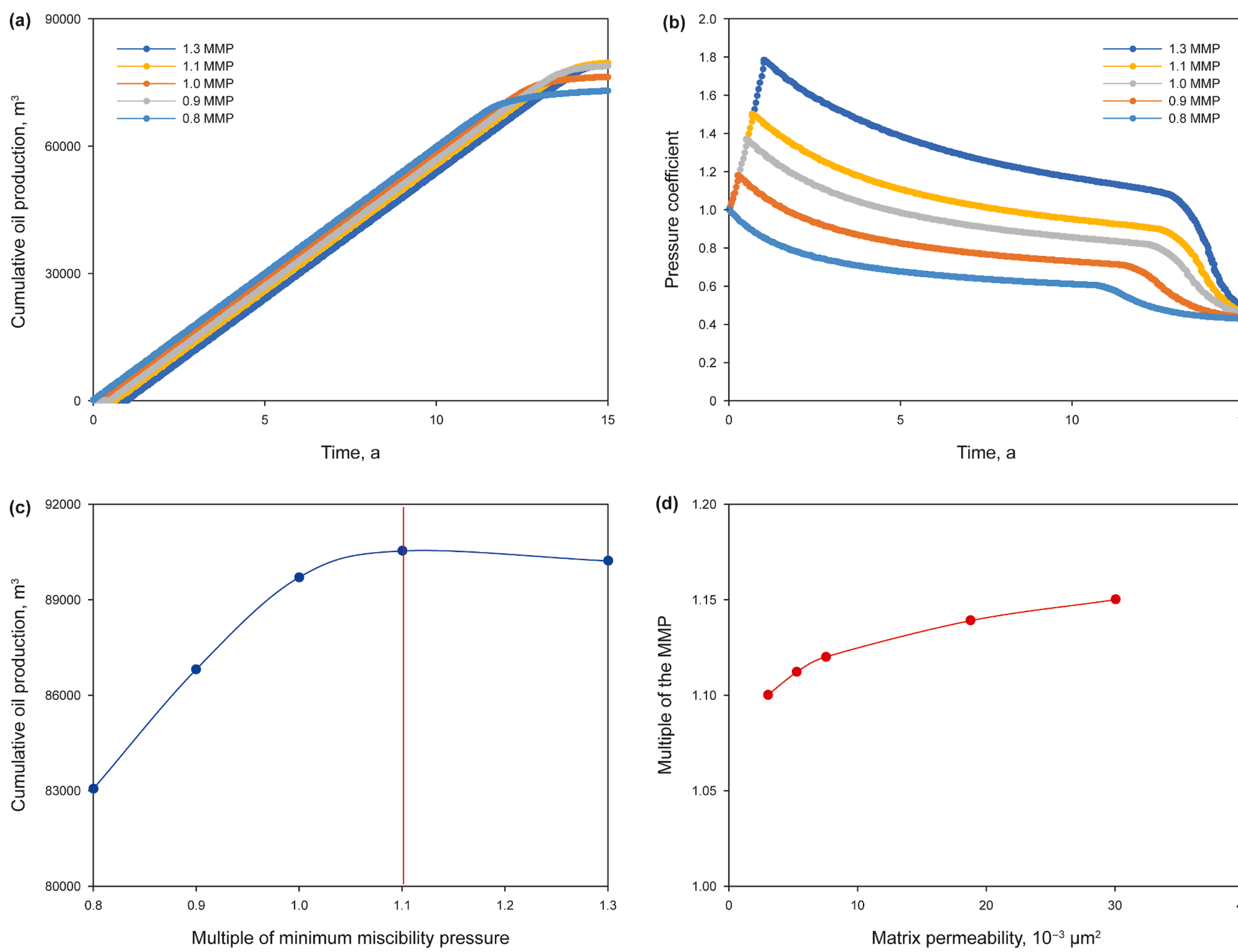

Fig. 22. Comparison of development effects under different reservoir pressure. Cumulative oil production versus time **(a)** and multiple of MMP **(c)**. **(b)** The reservoir pressure coefficient. **(d)** The recommended multiple of MMP.

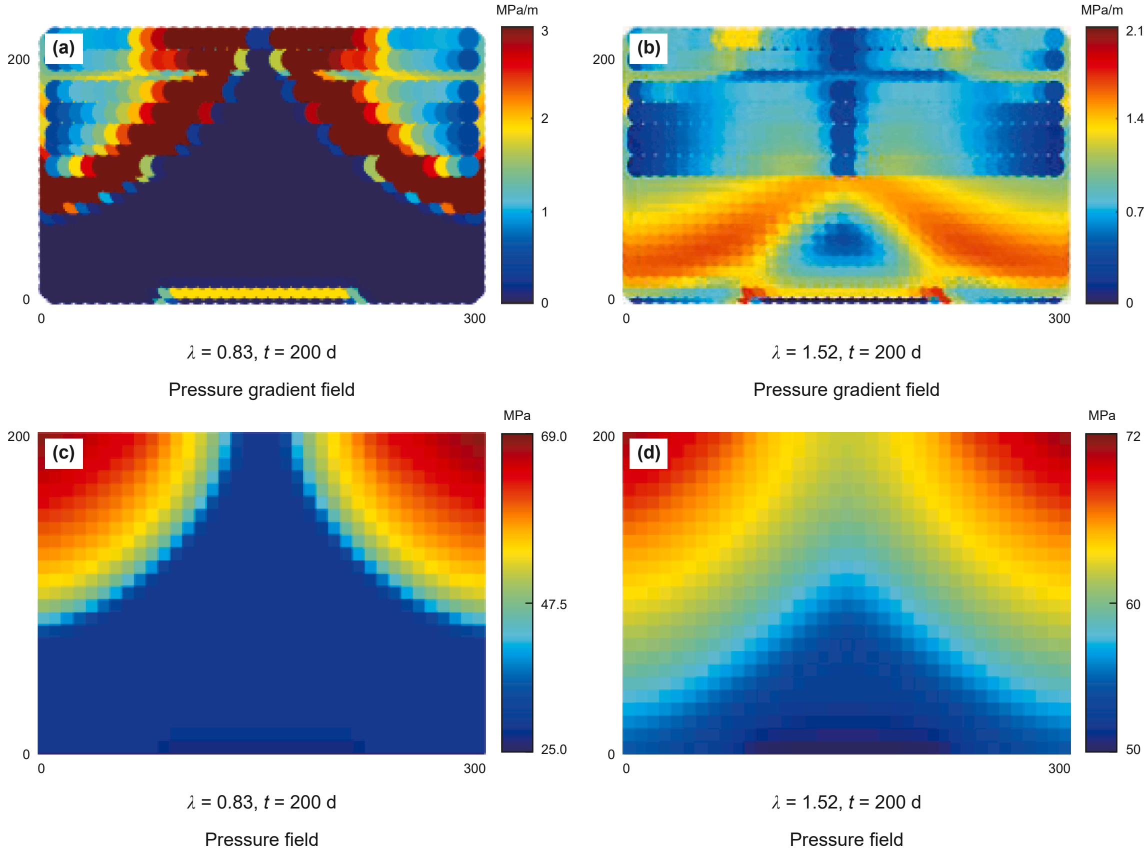

Fig. 23. Pressure gradient **(a, b)** and pressure **(c, d)** field comparison under different $\lambda = 0.83$ **(a, c)** and 1.52 **(b, d)** after 200 days waterflooding.

effect is strongly related to MMP. Therefore, $\lambda = 1.8, 1.5, 1.4, 1.2, 1.0$ equals to 1.3. 1.1, 1.0, 0.9, 0.8 multiple of the MMP. The cumulative oil production versus the multiple of MMP is drawn in Fig. 18(c) With the increase of the multiple of MMP, the cumulative oil production first increases significantly and then decreases slowly. As the pressure increases, the oil displacement efficiency is high. However, if the pressure increases further, gas channeling will reduce the production. The optimal value of the multiple of MMP is 1.1. The optimal values under different matrix permeability are investigated (Fig. 22(d)). As the matrix permeability increases, the optimal value gradually increases and then slows down.

3.3.2. *Injection timing optimization of H_2O flooding*

In waterflooding case, the reference reservoir pressure is set as 32 MPa. Matrix permeability is 5×10^{-3} μm^2. We investigate the displacement performance under different reservoir pressures. Fig. 23 compares the pressure gradient and pressure field under different λ. For $\lambda = 0.83$ (Fig. 23(a)–(c)). After 200 days displacement, the pressure and pressure gradient around the injection well are high and expand towards the production well in a fan shape. When the pressure gradient is greater than the true TPG, the oil could be effectively displaced. The effective displacement area is defined as the area where the pressure gradient is greater than the true TPG. Due to low reservoir pressure, the effect of matrix stress sensitivity is strong. The effective displacement area is only half of the total area. It is difficult to establish an effective displacement pressure system. While for $\lambda = 1.52$ (Fig. 23(b), (d)), the effect of matrix stress sensitivity is weak. The pressure front has reached the production well. The effective displacement area occupies the entire reservoir unit. It is easier and earlier to establish an effective displacement pressure system.

Fig. 24 quantitatively evaluate the production performance. As shown in Fig. 24(a), after the effective displacement pressure system is established, the cumulative oil production increases approximately linearly. While for different pressure coefficient, the establishment time of the effective displacement pressure system is different. The proportion of the effective displacement area is defined as the effective displacement area to the total area. Fig. 24(c) quantitatively evaluate the proportion of the effective displacement area. When the λ is 1.52, the time required to establish an effective displacement pressure system is 200 days. While for $\lambda = 0.83$, the time is 600 days. Therefore, the effect of matrix stress sensitivity significantly influences the early production. For the production after ~3000 days, as the λ increases from 0.83 to 1.52, the cumulative oil production first rises and then decreases (Fig. 24(b)). Due to the high λ, the effective displacement pressure system is established early, leading to an early water breakthrough time and severe ineffective water circulation. In this case, the λ corresponding to the optimal H_2O injection timing is 1.25. Furthermore, we have also investigated the recommended injection timing (λ) under different reservoir permeability. As shown in Fig. 24(d), as matrix permeability increases, the pressure coefficient corresponding to the recommended optimal water injection timing gradually decreases.

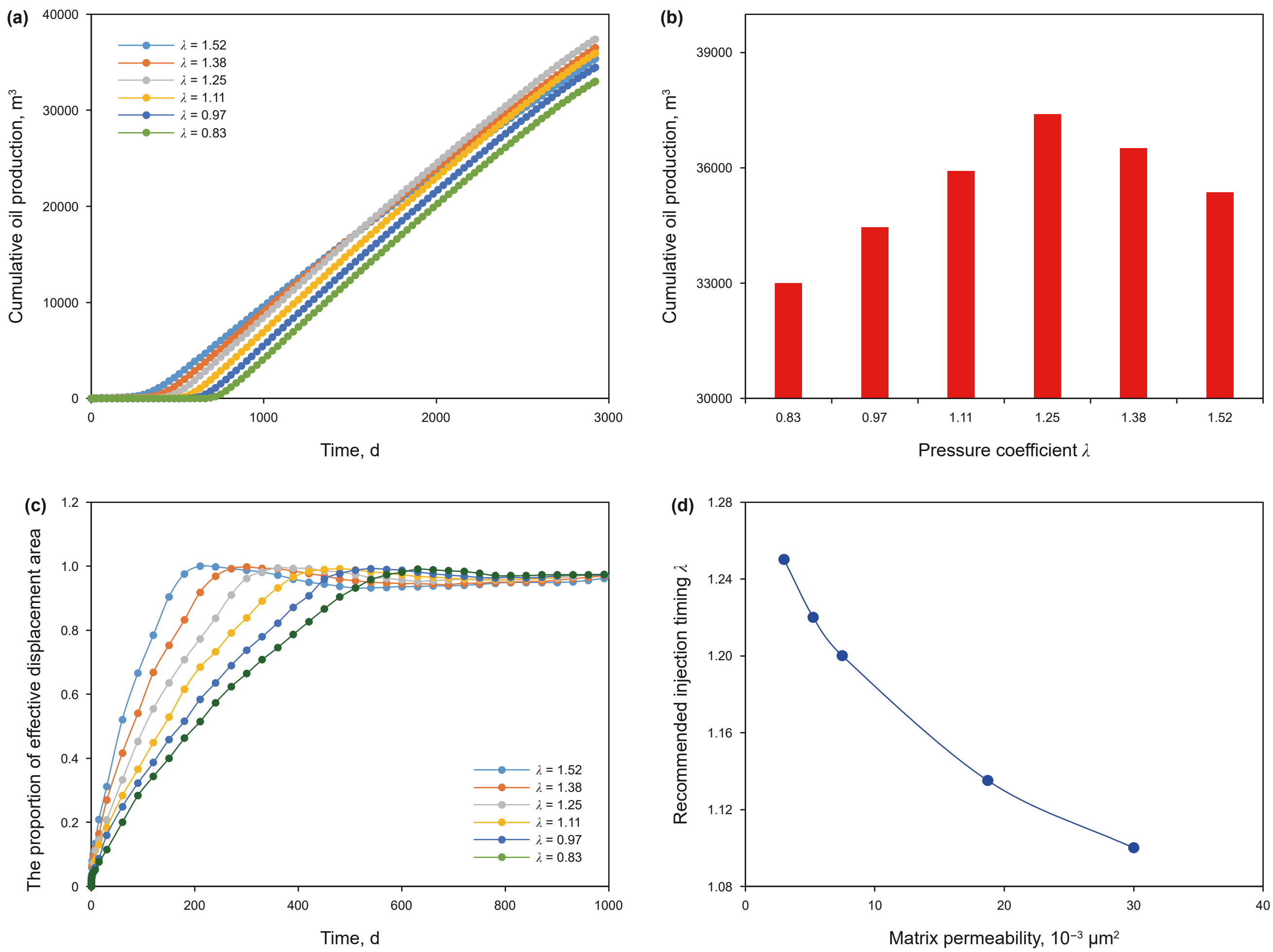

Fig. 24. Comparison of development effects under different reservoir pressure. Cumulative oil production versus time **(a)** and λ **(b)**. **(c)** The proportion of effective displacement area. **(d)** The recommended injection timing.

4. Conclusions

We built a compositional reservoir simulation method based on 3D-EDFM with multiple mechanisms. Then optimal design criterion and curve for injection fluid, rate, and timing are obtained. The role of low-velocity nonlinear flow, matrix stress sensitivity and CO_2 miscibility on injection rate or timing design cannot be neglected. It is recommended to adopt water injection for matrix permeability greater than 5×10^{-3} μm^2, and CO_2 injection for those with a matrix permeability lower than 5×10^{-3} μm^2. As injection rate increase, the cumulative oil production first increases and then slowly decreases. There exist optimal CO_2 and H_2O injection rates. In comparison with the traditional Darcy flow, the optimal H_2O injection rate is higher. The maximum difference of optimal injection rate reaches 11.1% with matrix permeability of 5×10^{-3} μm^2. As the matrix permeability increases, the reservoir pressure (corresponding to optimal CO_2 injection timing) gradually increases. While the pressure coefficient corresponding to the optimal H_2O injection timing gradually decreases. Our proposed 3D-EDFM compositional simulator can serve as an effective and reliable tool for injection-production optimization.

CRediT authorship contribution statement

Shi-Qian Xu: Writing – original draft, Investigation, Conceptualization. **Qi-Jun Zeng:** Investigation, Formal analysis. **Jian-Chun Guo:** Supervision, Conceptualization. **Rong-Hao Cui:** Writing – review & editing, Conceptualization. **Cong Lu:** Supervision, Funding acquisition. **Wen-Jian Zhou:** Software, Formal analysis. **Qin-Ru Xue:** Formal analysis.

Declaration of competing interest

The authors declare that they have no known competing financial interests or personal relationships that could have appeared to influence the work reported in this paper.

Acknowledgments

This work was partly supported by the National Natural Science Foundation of China (52304045); Natural Science Foundation of Sichuan Province (Youth Science Fund Category B) (2026NSFSC1333).

Nomenclature

ϕ	Porosity
ρ	The molar density of phase j, mol/m^3
ρ_o	The molar density of oil, mol/m^3
ρ_g	The molar density of gas, mol/m^3
ρ_w	The molar density of water, mol/m^3

S_j	The fluid saturation of phase j
ω_{ij}	The proportion of component i in the phase j
D_{ij}	Binary diffusion coefficient between component i and j in the mixture
t	The simulation time, s.
$\boldsymbol{v}_j$	Flow velocity of phase j, m/s
q_i	The sink/source term per unit reservoir volume of each component, mol/(m^3·s)
q_{inj}	The injection rate, m^3/d
P	The fluid pressure, Pa
G	The true TPG, Pa/m.
k	Matrix permeability, μm^2
μ	The fluid viscosity, mPa·s
δ_{rD}	Dimensionless residual boundary layer thickness
δ_{iD}	Dimensionless initial boundary layer thickness
c_φ	A coefficient of the nonlinear flow
k_m	The dynamic absolute matrix permeability, μm^2
k_{mi}	The initial absolute matrix permeability, μm^2
γ	The coefficient of matrix stress sensitivity
p_m	The dynamic fluid pressure in matrix pore, MPa
p_{mi}	The initial fluid pressure in matrix pore, MPa
$k_{\kappa,hf}$	Fracture permeability of the fluid κ, μm^2
F_c	The dynamic fracture conductivity, μm^2·cm
F_{ci}	The initial fracture conductivity, μm^2·cm
η_i	The dimensionless attenuation amplitude
η_r	The dimensionless residual fracture conductivity
C	A coefficient of the fracture conductivity attenuation
x_i	The molar fraction of composition i in oil phase
y_i	The molar fraction of composition i gas phase
z_i	The overall molar fraction of composition i
T_i	Half transmissibility of cell i
k_i	Permeability of cell i
A_i	Contact area of cell i
d_i	Vertical distance from center point to contact surface of cell i
$\mathbf{u}$	The vector containing optimization variables
N_p	The cumulative oil production
f_w	The water cut
R_s	The gas oil ratio
C	A constant value
q	The injection rate
t_{inj}	The injection timing

Subscript

κ	Oil or water
m	Matrix

References

Alhosani, A., Daraboina, N., 2021. Effect of multi-phase flow on asphaltene deposition: Field case application of integrated simulator. J. Petrol. Sci. Eng. 206, 108972. https://doi.org/10.1016/j.petrol.2021.108972.

Almasov, A., Onur, M., 2023. Life-cycle production optimization of the CO_2-water-alternating-gas injection process using least-squares support-vector regression proxy. SPE J. 28 (2), 715–736. https://doi.org/10.2118/210200-PA.

Asaadian, H., Ahmadi, P., Khormizi, M.Z., et al., 2022. Prevention of acid-induced sludge formation using an environmentally–friendly bio-based nonionic surfactant. J. Petrol. Sci. Eng. 218, 111009. https://doi.org/10.1016/j.petrol.2022.111009.

Azamipour, V., Assareh, M., Mittermeir, G.M., 2018. An improved optimization procedure for production and injection scheduling using a hybrid genetic algorithm. Chem. Eng. Res. Des. 131, 557–570. https://doi.org/10.1016/j.cherd.2017.11.022.

Bao, K., Lie, K.-A., Møyner, O., et al., 2017. Fully implicit simulation of polymer flooding with MRST. Comput. Geosci. 21 (5), 1219–1244. https://doi.org/10.1007/s10596-017-9624-5.

Behera, U.S., Sangwai, J.S., Baskaran, D., et al., 2024. A comprehensive review on low salinity water injection for enhanced oil recovery: Fundamental insights, laboratory and field studies, and economic aspects. Energy Fuels 39 (1), 72–103. https://doi.org/10.1021/acs.energyfuels.4c04562.

Ding, S., Wen, F., Wang, N., et al., 2022. Multi-objective optimization of CO_2 enhanced oil recovery and storage processes in low permeability reservoirs. Int. J. Greenh. Gas Control 121, 103802. https://doi.org/10.1016/j.ijggc.2022.103802.

Emami-Meybodi, H., Ma, M., Zhang, F., et al., 2024. Cyclic gas injection in low-permeability oil reservoirs: Progress in modeling and experiments. SPE J. 29 (11), 6217–6250. https://doi.org/10.2118/223116-PA.

Enab, K., Ertekin, T., 2021. Screening and optimization of CO_2-WAG injection and fish-bone well structures in low permeability reservoirs using artificial neural network. J. Petrol. Sci. Eng. 200, 108268. https://doi.org/10.1016/j.petrol.2020.108268.

Feng, Q., Xu, S., Xing, X., et al., 2020. Advances and challenges in shale oil development: A critical review. Adv. Geo-Energy Res. 4 (4), 406–418. https://doi.org/10.46690/ager.2020.04.06.

Gao, M., Liu, Z., Qian, S., et al., 2023. Machine-learning-based approach to optimize CO_2-WAG flooding in low permeability oil reservoirs. Energies 16 (17), 6149. https://doi.org/10.3390/en16176149.

Hu, W., Wei, Y., Bao, J., 2018. Development of the theory and technology for low permeability reservoirs in China. Petrol. Explor. Dev. 45 (4), 685–697. https://doi.org/10.11698/PED.2018.04.10.

Jiang, C., Chen, G., Zhu, W., et al., 2025. Numerical simulation and optimization design of complex underground fracture network. Adv. Geo-Energy Res. 16 (1), 1–3. https://doi.org/10.46690/ager.2025.04.01.

Jin, M., Ribeiro, A., Mackay, E., et al., 2016. Geochemical modelling of formation damage risk during CO_2 injection in saline aquifers. J. Nat. Gas Sci. Eng. 35, 703–719. https://doi.org/10.1016/j.jngse.2016.08.030.

Khurshid, I., Afgan, I., 2021. Investigation of water composition on formation damage and related energy recovery from geothermal reservoirs: geochemical and geomechanics insights. Energies 14 (21), 7415. https://doi.org/10.3390/en14217415.

Khurshid, I., Al-Shalabi, E.W., Afgan, I., et al., 2022. A numerical approach to investigate the impact of acid-asphaltene sludge formation on wormholing during carbonate acidizing. J. Energy Resour. Technol. 144 (6), 063001. https://doi.org/10.1115/1.4051738.

Lerlertpakdee, P., Jafarpour, B., Gildin, E., 2014. Efficient production optimization with flow-network models. SPE J. 19 (6), 1083–1095. https://doi.org/10.2118/170241-PA.

Li, J., Wei, J., Chen, Y., et al., 2024. Analysis of asynchronous/inter-fracture injection-production mechanism under the condition of five-spot vertical and horizontal well combination in low permeability oil reservoirs. Energy 308, 132923. https://doi.org/10.1016/j.energy.2024.132923.

Li, S., Zhang, K., Jia, N., et al., 2018. Evaluation of four CO_2 injection schemes for unlocking oils from low-permeability formations under immiscible conditions. Fuel 234, 814–823. https://doi.org/10.1016/j.fuel.2018.07.052.

Lie, K.A., Krogstad, S., Ligaarden, I.S., et al., 2012. Open-source MATLAB implementation of consistent discretisations on complex grids. Comput. Geosci. 16, 297–322. https://doi.org/10.1007/s10596-011-9244-4.

Liu, P., Zhang, X., Hao, M., et al., 2016. Parameter optimization of gas alternative water for CO_2 flooding in low permeability hydrocarbon reservoirs. J. Renew. Sustain. Energy 8 (3), 035901. https://doi.org/10.1063/1.4948483.

Liu, Z., Forouzanfar, F., Zhao, Y., 2018. Comparison of SQP and AL algorithms for deterministic constrained production optimization of hydrocarbon reservoirs. J. Petrol. Sci. Eng. 171, 542–557. https://doi.org/10.1016/j.petrol.2018.06.063.

Lyu, W., Zeng, L., Chen, M., et al., 2018. An approach for determining the water injection pressure of low-permeability reservoirs. Energy Explor. Exploit. 36 (5), 1210–1228. https://doi.org/10.1177/0144598718754374.

Meng, S., Fu, Q., Tao, J., et al., 2024. Predicting CO_2-EOR and storage in low-permeability reservoirs with deep learning-based surrogate flow models. Geoenergy Sci. Eng. 233, 212467. https://doi.org/10.1016/j.geoen.2023.212467.

Ren, G., Jiang, J., Younis, R.M., 2018. A model for coupled geomechanics and multiphase flow in fractured porous media using embedded meshes. Adv. Water Resour. 122, 113–130. https://doi.org/10.1016/j.advwatres.2018.09.017.

Rui, Z., Deng, H., Hu, T., et al., 2025. Coupling mechanism analysis of CO_2 non-darcy flow in multi-scale reservoirs: a case study of the life-cycle process of fracturing-development in shale oil reservoirs. Pet. Sci. 22 (3), 1171–1199. https://doi.org/10.1016/j.petsci.2024.12.018.

Sæle, A.M., Graue, A., Alcorn, Z.P., 2022. Unsteady-state CO_2 foam injection for increasing enhanced oil recovery and carbon storage potential. Adv. Geo-Energy Res. 6 (6), 472–481. https://doi.org/10.46690/ager.2022.06.04.

Song, F., Bo, L., Zhang, S., et al., 2019. Nonlinear flow in low permeability reservoirs: modelling and experimental verification. Adv. Geo-Energy Res. 3 (1), 76–81. https://doi.org/10.26804/ager.2019.01.06.

Sun, F., Xu, W., Jiang, W., et al., 2024. Progress and prospects of CNOOC's low permeability and unconventional oil and gas reservoir stimulation technologies. China Offshore Oil Gas 36 (1), 109–116. https://doi.org/10.11935/j.issn.1673-1506.2024.01.011 (in Chinese).

Sun, X., Zhang, Y., Wu, J., et al., 2019. Optimized cyclic water injection strategy for oil recovery in low-permeability reservoirs. J. Energy Resour. Technol. 141 (1), 012905. https://doi.org/10.1115/1.4040751.

Tian, Y., Uzun, O., Shen, Y., et al., 2020. Feasibility study of gas injection in low permeability reservoirs of changqing oilfield. Fuel 274, 117831. https://doi.org/10.1016/j.fuel.2020.117831.

Wang, L., Zhang, H., Peng, X., et al., 2019. Water-sensitive damage mechanism and the injection water source optimization of low permeability sandy conglomerate reservoirs. Petrol. Explor. Dev. 46 (6), 1218–1230. https://doi.org/10.1016/S1876-3804(19)60275-2.

Wang, J., Liu, J., Zhaoguo, L., et al., 2020. Synchronous injection-production energy replenishment for a horizontal well in an ultra-low permeability sandstone reservoir: A case study of Changqing oilfield in Ordos Basin, NW China. Petrol. Explor. Dev. 47 (4), 827–835. https://doi.org/10.1016/S1876-3804(20)60098-2.
Wang, M., Dong, L., Chen, F., et al., 2022. Study on the optimization of injection modes and injection parameters for natural gas in ultra-low permeability reservoir. Energy Rep. 8, 232–238. https://doi.org/10.1016/j.egyr.2022.03.114.
Wang, S., Zhang, M., Zhang, Y., et al., 2025a. Mechanisms of CO_2 huff and puff enhanced oil recovery and storage within shale nanopores. Chem. Eng. J., 160098 https://doi.org/10.1016/j.cej.2025.160098.
Wang, S., Chen, L., Feng, Q., et al., 2025b. Lattice Boltzmann simulation of pre-darcy flow in porous media. Geoenergy Sci. Eng. 250, 213852. https://doi.org/10.1016/j.geoen.2025.213852.
Wang, S., Qin, C., Feng, Q., et al., 2021. A framework for predicting the production performance of unconventional resources using deep learning. Appl. Energy 295, 117016. https://doi.org/10.1016/j.apenergy.2021.117016.
Wang, X., Wang, P., Tang, K., et al., 2024. Optimization of carbon sequestration and carbon displacement in fractured horizontal wells in low permeability reservoirs. Processes 12 (1), 145. https://doi.org/10.3390/pr12010145.
Wang, X., Dang, H., Gao, T., 2018. Method of moderate water injection and its application in ultra-low permeability oil reservoirs of Yanchang Oilfield, NW China. Petrol. Explor. Dev. 45 (6), 1094–1102. https://doi.org/10.11698/PED.2018.06.10.
Xiao, P., Yang, Z., Wang, X., et al., 2017. Experimental investigation on CO_2 injection in the Daqing extra/ultra-low permeability reservoir. J. Petrol. Sci. Eng. 149, 765–771. https://doi.org/10.1016/j.petrol.2016.11.020.
Xiong, S., Chu, S., He, Y., et al., 2018. Water quality optimization for effective water injection into low permeability reservoirs. Spec. Top Rev. Porous Media Int. J. 9 (1), 27–36. https://doi.org/10.1615/SpecialTopicsRevPorousMedia.2017020340.
Xu, S., Ren, G., Younis, R.M., et al., 2021. Revisiting field estimates for carbon dioxide storage in depleted shale gas reservoirs: the role of geomechanics. Int. J. Greenh. Gas Control 105, 103222. https://doi.org/10.1016/j.ijggc.2020.103222.
Xu, S., Guo, J., Feng, Q., et al., 2022. Optimization of hydraulic fracturing treatment parameters to maximize economic benefit in tight oil. Fuel 329, 125329. https://doi.org/10.1016/j.fuel.2022.125329.
Xu, S., Wang, S., Guo, J., et al., 2025a. Optimization of vertical well pattern and hydraulic fracture in offshore low-permeability reservoir: the role of low-velocity nonlinear flow. SPE J. 30 (12), 7893–7909. https://doi.org/10.2118/231171-PA.
Xu, S., Zhang, X., Guo, J., et al., 2025b. Nonlinear flow mechanism and production characteristics of thin interbedded tight oil reservoirs. Phys. Fluids 37 (1), 016621. https://doi.org/10.1063/5.0247381.
Yan, X., Qin, G.Y., Zhang, L.M., et al., 2024. A dual-porosity flow-net model for simulating water-flooding in low-permeability fractured reservoirs. Geoenergy Sci. Eng. 240, 213069. https://doi.org/10.1016/j.geoen.2024.213069.
Yang, R., Zhang, W., Liu, S., et al., 2025. Multi-objective optimization workflow for CO_2 water-alternating-gas injection assisted by single-objective pre-search. Pet. Sci. 22 (7), 2967–2976. https://doi.org/10.1016/j.petsci.2025.03.038.
Yang, R., Zhang, L., Tan, X., et al., 2024. Study on different miscibility intervals of an impure CO_2-crude oil system in offshore low-permeability reservoirs. Energy Fuels 38 (2), 1010–1018. https://doi.org/10.1021/acs.energyfuels.3c03884.
Zhang, L., Li, C., Zhang, Y., et al., 2024. CO_2-EOR and storage in a low-permeability oil reservoir: optimization of CO_2 balanced displacement from lab experiment to numerical simulation. Geoenergy Sci. Eng. 243, 213325. https://doi.org/10.1016/j.geoen.2024.213325.
Zhang, L., Tian, P., Xing, C., et al., 2021. Best practices in development and production optimization of offshore low permeability reservoir. In: SPE Asia Pacific Oil and Gas Conference and Exhibition. SPE. https://doi.org/10.2118/205613-MS.
Zhao, J., Fan, J., He, Y., et al., 2015. Optimization of horizontal well injection-production parameters for ultra-low permeable–tight oil production: A case from Changqing Oilfield, Ordos Basin, NW China. Petrol. Explor. Dev. 42 (1), 74–82. https://doi.org/10.1016/S1876-3804(15)60008-8.
Zhao, Z., Jiang, S., Lei, T., et al., 2025. Optimization of key parameters of fracturing flooding development in offshore reservoirs with low permeability based on numerical modeling approach. J. Mar. Sci. Eng. 13 (2), 282. https://doi.org/10.3390/jmse13020282.
Zhou, Y., Lei, S., Du, X., et al., 2021. Injection-production optimization of carbonate reservoir based on an inter-well connectivity model. Energy Explor. Exploit. 39 (5), 1666–1684. https://doi.org/10.1177/0144598721994653.